Geochemical Perspectives Letters

The journey of K-MORBs, told through geological, geochemical and geophysical data

L. Grenet[1,2,3,#*], C. Hamelin[4], D. Brunelli[5,6,7], M. Maia[1], A. Briais[1], L. Verhoest[5,1], Z. Yu[8,1,2], S.C. Singh[2]

https://doi.org/10.7185/geochemlet.2612

Abstract

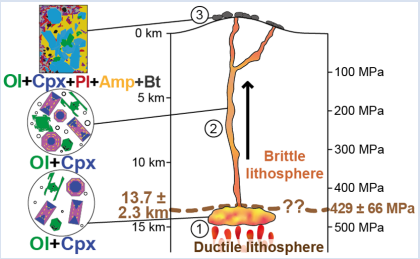

The compositional variability of mid-ocean ridge basalts (MORBs) stems from a combination of the heterogeneity of the mantle source, magma mixing, and partial crystallisation of magma in the lower crust. These variations have been mainly explored at the global and ridge scales, with only a few studies investigating them at the kilometre scale and below. Here, we focus on a series of tholeiitic to K-rich basalt samples collected during a single submarine dive near the eastern intersection between the Mid-Atlantic Ridge and the Romanche transform fault, in the equatorial Atlantic. The geochemical and petrological variations, attributed to variations in melting conditions, are extreme and consistent with the geological features. Clinopyroxene phenocrysts present in certain K-rich basalts, recorded the history of magma storage. We calculated the crystallisation pressures of clinopyroxenes and compared them to microseismicity depths recorded in the area, thus providing constraints on the lithospheric structure. This multidisciplinary work highlights the interest in exploring the composition of MORBs at high resolution to better understand the construction of the oceanic crust.

Received 25 August 2025 | Accepted 5 March 2026 | Published 13 April 2026

Introduction and Geological Context

The Mid-Atlantic Ridge (MAR) is offset by numerous transform faults (TFs) in the equatorial zone, including the large Romanche TF. The latter offsets the ridge axis by 900 km (Fig. 1a), resulting in a lithospheric age contrast of ~45 Ma and a strong cold-edge effect (Schilling *et al.*, 1994, 1995; Bonatti *et al.*, 1996, 2001; Ligi *et al.*, 2005). In addition to the local effect of the TF, the regional average temperature of the equatorial upper mantle is colder than in adjacent regions (Schilling *et al.*, 1994, 1995). A recent study based on seismic data has highlighted the presence of a thinner-than-normal crust, near the Romanche transform fault intersection with the MAR (Gregory *et al.*, 2021). Due to the combination of local and regional temperature anomalies, the degree of mantle partial melting and magma production decrease along the axis (Brunelli *et al.*, 2025), whereas lithosphere thickness increases approaching the TF (Ligi *et al.*, 2005). Basalts sampled along the ridge segments at the Eastern Romanche Ridge Transform Intersection (ERRTI) present extreme compositional variability from tholeiitic to alkaline basalts (Schilling *et al.*, 1994, 1995; Le Voyer *et al.*, 2015; Brunelli *et al.*, 2025). Brunelli *et al.* (2025) suggest that the enriched basalts are produced by reduced extents of melting of a composite mantle, where low solidus pyroxenites are dispersed in a depleted mantle. Those components may have originated from ancient dismembered sedimented oceanic crust dispersed in the mantle or from filaments of subducted oceanic plate incorporated into an ascending hot plume (Brunelli *et al.*, 2025). The processes of generation and migration of different magmas at a local scale remain poorly understood due to a lack of studies based on detailed and dense sampling.

During the SMARTIES cruise (Maia *et al.*, 2019), we explored the ERRTI volcano-tectonic setting and investigated the origin and formation of the alkaline water-rich magmas observed in the region. We focused on dive SMA1974, combining geological, geochemical, and geophysical datasets. Geochemical sampling along this dive revealed extreme variations in compositions ranging from tholeiitic to potassium-rich alkaline basalts, accompanying the variations in volcanic edifice morphology (Figs. 1, S-1). The alkaline basalts contain clinopyroxene phenocrysts, which were used in geobarometry calculations to explore the magma storage history.

1. Geo-Ocean, UMR6538 CNRS-IFREMER-UBO-UBS Institut, Universitaire Européen de la Mer IUEM, Brest, France
2. Université Paris Cité, Institut de Physique du Globe de Paris, CNRS, UMR 7154, 75005 Paris, France
3. Université de La Réunion, Laboratoire GéoSciences Réunion, CNRS, UMR 7154, 97744 Saint-Denis, France
4. Independent scholar, Sondre Skogveien 7, 5055 Bergen, Norway
5. Dipartimento di Scienze Chimiche e Geologiche, Università di Modena e Reggio Emilia, 41125 Modena, Italy
6. Woods Hole Oceanographic Institution, Woods Hole, 02543-1050 MA, USA
7. Istituto di Geologia Ambientale e Geoingegneria CNR, 00185 Roma, Italy
8. State Key Laboratory of Submarine Geoscience, Second Institute of Oceanography, Ministry of Natural Resources, Hangzhou 310012, China

Now at [2, 3]

* Corresponding author (email: lea.grenet@univ-reunion.fr)

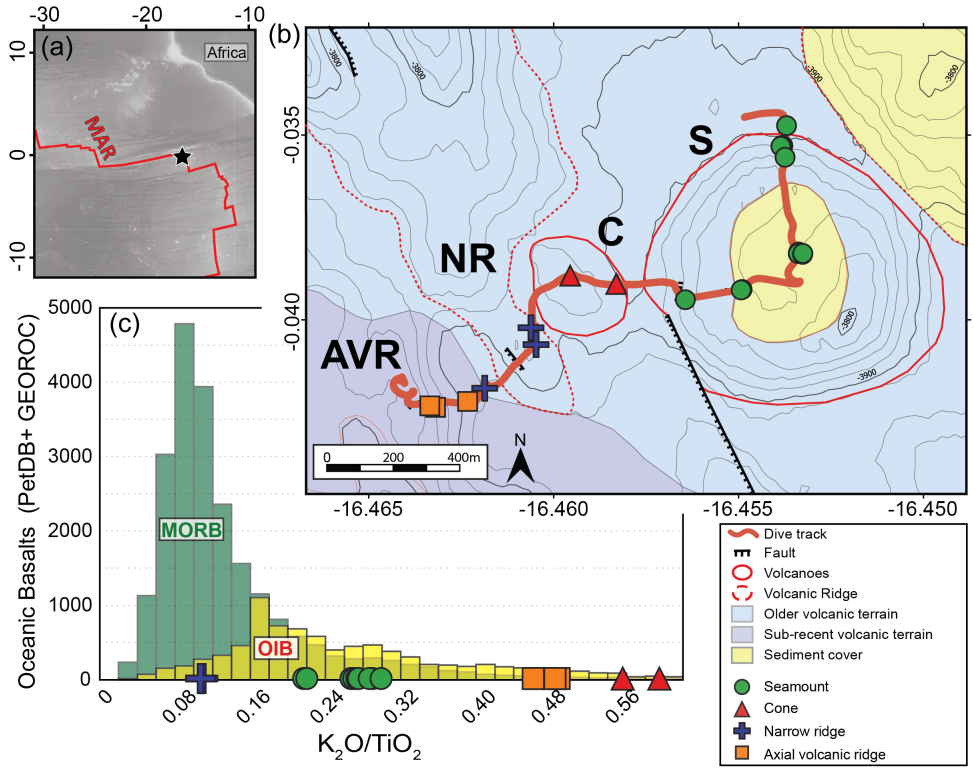

Figure 1 **(a)** Location of the ERRTI (black star). **(b)** Geological map of dive SMA1974 with the locations of the samples. S: seamount; C: cone; NR: narrow ridge; AVR: axial volcanic ridge (modified from Grenet *et al.*, 2025). **(c)** K_2O/TiO_2 ratio in samples from dive SMA1974 compared to the frequency occurrences of global mid-oceanic ridge basalts (MORB, green) and ocean island basalts (OIB, yellow) from PetDB and GEOROC datasets. Seamount and AVR data are from Brunelli *et al.* (2025).

By combining geological, geochemical, petrological, and geophysical data obtained over a small sampling area, this study provides new perspectives on our understanding of the distribution of MORB compositions through space and time and their storage conditions.

Dive SMA1974 Dataset

The ~2 km-long SMA1974 submersible dive was conducted 40 km south of the ERRTI, extending from the eastern part of the rift valley floor to the eastern flank of the axial volcanic ridge (AVR), and explored four distinct volcanic edifices: a flat-topped seamount, a small cone, a narrow volcanic ridge, and the main AVR (Figs. 1b, S-1, S-2). The cone was dated by the $^{40}Ar/^{39}Ar$ method to 135.3 ± 11.1 ka and appears to be contemporaneous with the seamount and the ridge, while the AVR seems more recent (Grenet *et al.*, 2025).

We present whole rock major and trace element analyses carried out by an inductively coupled plasma-atomic emission spectrometer and by a high-resolution inductively coupled plasma mass spectrometer, respectively. *In situ* major and trace analyses of individual minerals were performed, on polished thin sections, by electron probe microanalysis (EPMA) and laser ablation inductively coupled mass spectrometer, respectively. Geochemical maps of the samples were obtained by EPMA. The geochemical methods and thermobarometric calculations, performed on ten clinopyroxenes, are described in the Supplementary Information. Analyses of the composition of the seamount and AVR glasses were carried out by Brunelli *et al.* (2025).

Whole rock and petrological compositions. The four volcanic edifices identified during the dive have distinct petrological and geochemical characteristics (Fig. 1b-c). The narrow ridge samples are tholeiitic, while those from the cone are alkaline basalts (Figs. S-3, S-4). The samples from the seamount and the AVR have intermediate compositions. The K_2O/TiO_2 ratios of the SMA1974 dive samples extend over the entire range of global ocean basalt databases (including MORBs and OIBs, Fig. 1c).

Lavas studied here are classified as N-MORB, E-MORB, and K-MORB according to Brunelli *et al.* (2025). Samples defined as K-MORB represent a peculiar group of alkali-rich basalts reaching true alkaline, nepheline-normative compositions (Brunelli *et al.*, 2025). If oceanic basalts enriched in sodium are common in ridge settings with low degrees of partial melting, the K-MORB samples stand out because of their enrichment in potassium (Fig. S-5a). The samples from the cone and the AVR are K-MORBs (Fig. 1c), while those from the narrow ridge and the seamount are N-MORBs and E-MORBs, respectively. Trace element patterns are coherent with major elements and can be separated into distinct groups corresponding to each geological edifice (Figs. 2, S-5b and S-6).

While the tholeiitic and intermediate samples have petrological textures often observed in MORBs (aphyric to sparsely plagioclase-phyric basalts), K-MORB samples from the cone exhibit characteristics of alkali basalts. They are microlithic basalts, containing euhedral clinopyroxene phenocrysts, a low proportion of skeletal olivine phenocrysts, and hydrated, K-rich mineral phases, namely microliths of amphiboles and biotites (Figs. S-8, S-9). We also note the absence of plagioclase phenocrysts in these samples (see detailed descriptions in the Supplementary Information).

Clinopyroxene geochemistry. The clinopyroxene phenocrysts display prominent sector zoning. The hourglass sectors

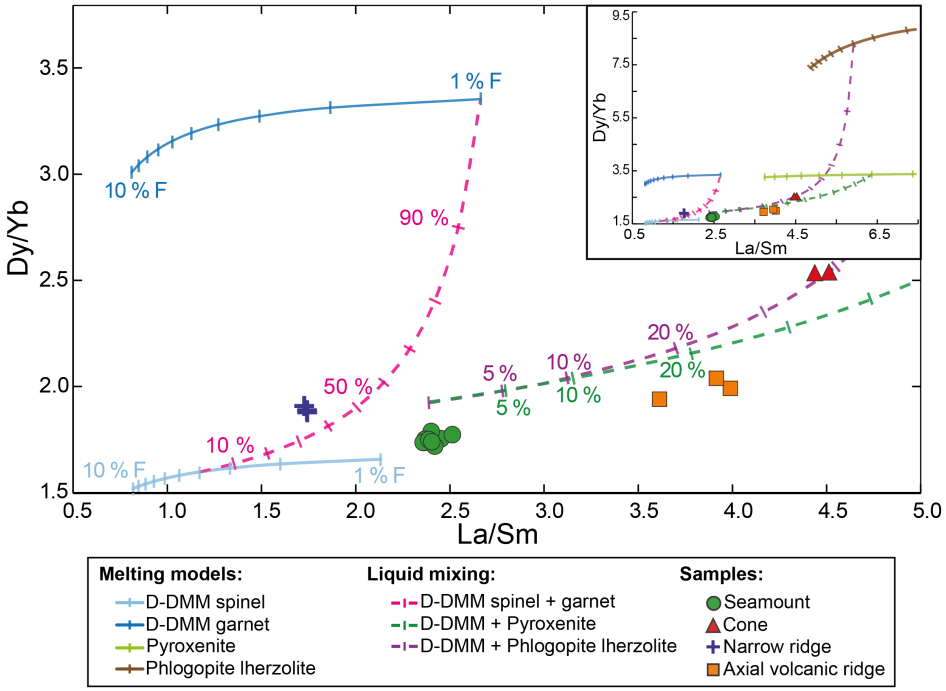

Figure 2 Plot of Dy/Yb *vs.* La/Sm for samples from dive SMA1974. Solid lines represent melting models: in blue, D-DMM in the spinel and garnet stability fields (Workman and Hart, 2005); in brown, phlogopite-bearing lherzolite in the spinel stability field (Grégoire *et al.*, 2002); and in light green, pyroxenite in the garnet stability field (G2, from Lambart, 2017). Dashed lines represent examples of liquid mixing between those melts. The parameters used are detailed in Table S-1.

have compositions enriched in Si-Mg, while the prism sectors are Al-Ti-rich (Fig. 3). Al- and Ti-rich sectors are enriched in rare earth elements and high field strength elements compared to Si-Mg-rich sectors (Table S-5).

On EPMA profiles, Cr_2O_3 peaks are observed, reaching 0.6 ± 0.006 to 1.2 ± 0.012 wt. % (Tables S-7 to S-18). These Cr peaks correlate with an increase in compatible elements (SiO_2 and MgO) and a decrease in incompatible elements (Al_2O_3 and TiO_2) compared to regular compositions (Fig. 3). Independent of the crystal sector-zoning and Cr_2O_3 peaks, concentric bands enriched in Cr_2O_3 can be observed in the geochemical maps (Fig. 3a).

Thermobarometry. The crystallisation temperatures and pressures of clinopyroxenes were iteratively estimated using Equation 33 in Putirka (2008) and Equation 1 in Neave and Putirka (2017), respectively. The equilibrium between clinopyroxenes and the whole rock was tested and considered to be reached for a $K_D = 0.03 \pm 0.08$ (Equation 35 in Putirka, 2008; Wieser *et al.*, 2023a). Component equilibria ΔDiHd, ΔEnFs, and ΔCaTs were tested using thresholds of 0.06, 0.05, and 0.03, respectively (Mollo *et al.*, 2013). The procedure was applied to the SMA1974-279 glass to evaluate the suitability of whole rock compositions for equilibrium testing. Comparable results between glass and whole rock data support the use of the latter for subsequent calculations (Table S-19). According to Zhou *et al.* (2021), in sector-zoned clinopyroxenes, the SiO_2-rich sectors are closer to real equilibrium than Al_2O_3-rich sectors. Hence, only analyses undertaken in Si-Mg-rich sectors were kept for P–T interpretations.

Melt H_2O contents were estimated using the MORB H_2O/Ce ratio from the database of Le Voyer *et al.* (2015), yielding values of 1.48 wt. % for SMA1974-278 and 1.47 wt. % for SMA1974-279.

Ten clinopyroxenes, from SMA1974-278 and SMA1974-279, satisfied all equilibrium criteria and were used for thermobarometric calculations (Figs. S-13 to S-18). Calculated temperatures range from 1112.9 to 1174.4 ± 45 °C, and pressures from 1.0 to 5.5 ± 3.8 kbar, with an average of 2.9 ± 0.9 kbar (Table S-20).

The results obtained with clinopyroxene barometers should be used with caution. Wieser *et al.* (2023a,b) highlighted the fact that these models allow only a rough distinction between crustal zones. They pointed out that considerable uncertainties arise in pressure calculations due to analytical errors related to the measurement of glass and clinopyroxene compositions and their compositional variability. To limit the effect of these errors, we tested different equilibrium criteria and used the average of at least five analysis points to obtain the crystallisation pressure of each crystal. In addition, we chose the Neave and Putirka (2017) barometer because their database is based on the analysis of >5 clinopyroxenes and is composed of Icelandic samples whose compositions are close to that of the cone (Wieser *et al.*, 2023a,b).

Discussion

Global basalt compositional variability expressed on a local scale. The range of K_2O/TiO_2 ratios along the 2-km-long SMA1974 dive is almost as large as that of global oceanic basalts (Fig. 1c). To explore which source compositions and melting conditions could account for this local geochemical variability, we calculated melting curve paths derived from non-modal batch melting involving different source compositions (Fig. 2) using Equation 15 from Shaw (2000).

The composition of the alkaline lavas cannot be accounted for by extremely low degree melting of a D-DMM source. Instead, as proposed by Verhoest (2022) and Brunelli *et al.* (2025), the generation of K-MORB requires the involvement of a pyroxenite component in the mantle source (20–40 %). Furthermore, the elevated K and H_2O contents suggest the

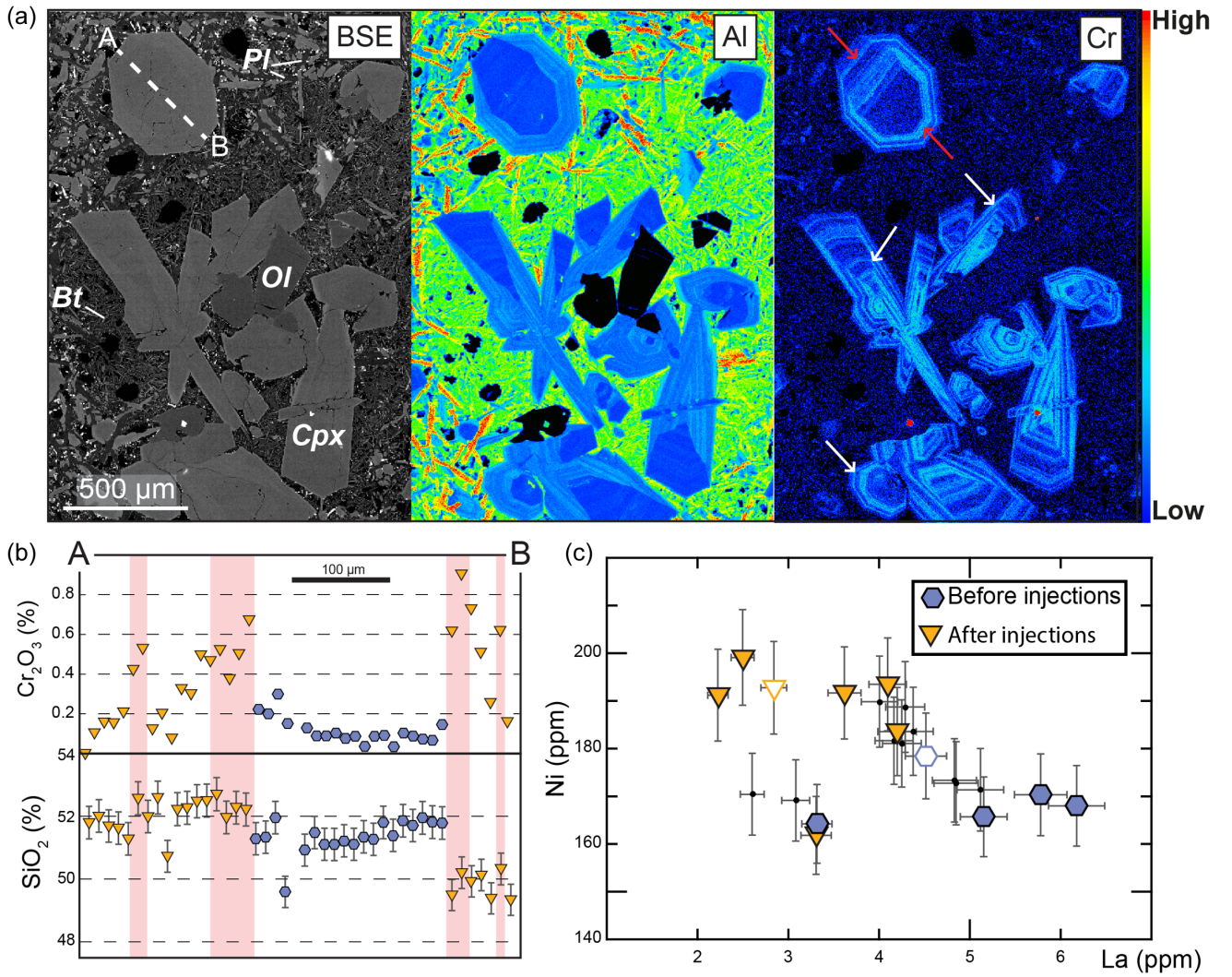

Figure 3 Major and trace element analyses of clinopyroxenes. **(a)** Left: Backscatter electron (BSE) image of a glomerophyre in SMA1974-279. The dashed line marks the trace of the profile analysis in (b). Cpx: clinopyroxene; Ol: olivine; Pl: plagioclase; Bt: biotite. Centre and right: Al and Cr element content maps, obtained by EPMA. The red arrows show the Cr_2O_3 peaks observed along the profile in (b). The white arrows present oscillatory zonation. **(b)** Cr_2O_3 and SiO_2 contents along the A–B profile. Error bars represent 1 % of the value obtained. The red bands represent the Cr_2O_3 peaks. Measurements taken with 10 µm steps. **(c)** Ni *vs.* La diagram separating analyses before and after Cr_2O_3 peaks.

presence of hydrated minerals in the K-MORB source, such as phlogopite or amphibole. Our models indicate that magma from the cone results from a mixing of melts including ~40 % liquid from melting of a phlogopite-bearing lherzolite.

These models suggest that the pronounced geochemical variability observed in SMA1974 reflects temporal changes in melting conditions of a heterogeneous mantle. Such variations occurred coevally or within a time span shorter than 135.3 ± 11.1 kyr (the estimated age of the cone).

The alkaline basalts dredged near the ERRTI also exhibit elevated volatile contents (Le Voyer *et al.*, 2015; Yu *et al.*, 2025). The high average water content (~1.5 wt. %) inferred from the H_2O/Ce ratio (Le Voyer *et al.*, 2015), support this interpretation. The elevated water content could be derived either from the mantle source itself or from the assimilation of seawater-altered crustal material. To evaluate this, we examined geochemical proxies of seawater contamination such as Cl/Nb and Cl/K in basalt glasses (Leroux *et al.*, 2006). Small contributions of seawater, linked to the source composition or by assimilation of altered crust material, would increase Cl concentration within the melt. However, all samples from dive SMA1974 have normal mantle Cl values (Cl/Nb < 22, Fig. S-10 and Cl/K < 0.08). Consistent with our melting models, these results indicate that the elevated water contents in K-MORBs reflect source heterogeneity rather than secondary contamination. Further analyses of the volatile contents of glass (H_2O, Cl and F) are required to settle this debate.

From the magmatic reservoir to the seafloor. The occurrence of clinopyroxene in basalts from the cone provides key constraints on the crystallisation and pre-eruptive evolution of these magmas. These crystals preserve the compositional record of their storage conditions during their growth. Variations in clinopyroxene Cr_2O_3 contents reveal two distinct patterns: broad Cr_2O_3-rich peaks and thin oscillatory zonation (Figs. 3 and S-11).

The high Cr_2O_3 peaks coincide with a decrease in incompatible element concentrations and enrichment in compatible elements, consistent with magma recharge by a more primitive melt (Ubide *et al.*, 2019). Nickel concentration increases immediately after Cr_2O_3-rich peaks, whereas lanthanum content decreases slightly (Fig. 3c), suggesting that the injected magma was less enriched in trace elements. The presence of pronounced sectoral zoning in clinopyroxenes, as described by MacDonald *et al.* (2024), further supports magma mixing and recharge as key processes.

The second type of Cr_2O_3 variation is thinner oscillatory zonation, not correlated with variations in compatible major elements (Fig. 3a). Crystallisation experiments show that active convection supplies fresh Cr-cations to the melt–crystal interface, which are incorporated into low-amplitude concentric bonds (Di Fiore *et al.*, 2021). This observation suggests that those clinopyroxenes crystallised in a dynamic convective reservoir (Petrone *et al.*, 2022).

Estimation of the lithosphere brittle–ductile boundary depth: agreement between geochemistry and geophysics. We took advantage of the presence of clinopyroxenes in the cone samples to estimate their crystallisation pressure and compare our results to the depths estimated by microseismicity. Given the limited number of clinopyroxenes analysed, the use of whole rock composition, the limits of the barometers, and the fact that the seismic data was only collected over a short period, further work is needed to confirm these depths on a regional scale.

Microseismicity recorded by ocean bottom seismometers (OBS) in this segment (Yu *et al.*, 2025), shows some events with focal depths between 9.1 ± 3.3 km and 19.3 ± 4.3 km below the seafloor (Figs. 4 and S-2). This is deeper than would be expected (<8 km) under regular slow-spreading ridges (Grevemeyer *et al.*, 2019). Based on the basalt chemical composition in samples from this segment, Yu *et al.* (2025) predicted a high concentration of volatiles in primary melts in this region and proposed CO_2 exsolution in deep melts as a potential origin of the deep microseismicity.

Since we do not know the exact proportion of volcanic crust and lithospheric mantle in our region, we calculated the crystallisation depths using densities of 2.8 g/cm^3 (basalt-dominated lithosphere) and 3.3 g/cm^3 (ultramafic lithosphere). We acknowledge that a realistic value should be somewhere in between. The calculated crystallisation depths range from 6.2 ± 2.6 km to 13.8 ± 2.3 km below the seafloor (Fig. 4, Table S-20). The variability in crystallisation depths could be due to the magma stagnating at different levels, possibly in small pockets, on its way to the surface. These depths are consistent with the current depth of microseismicity located between four and six kilometres west to southwest of the cone (Figs. 4 and S-2).

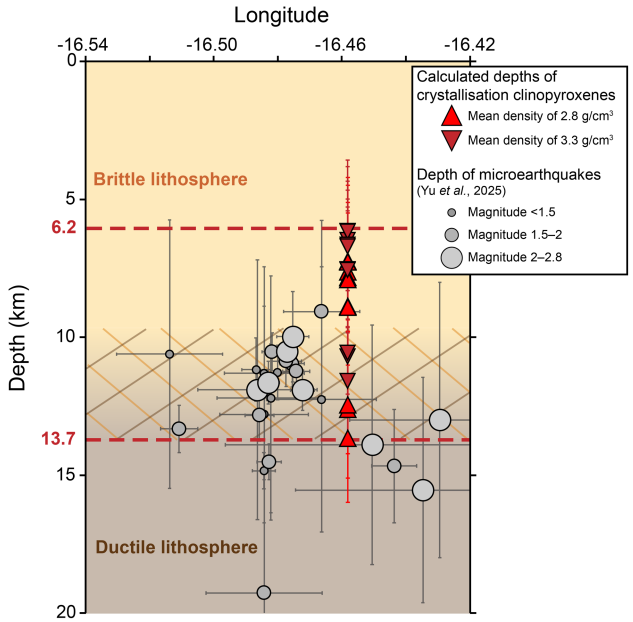

Figure 4 Calculated crystallisation depths of clinopyroxenes and microearthquake depths (Yu *et al.*, 2025), plotted according to longitude. The composition of the ten clinopyroxenes was measured at different points on each of the minerals. The average depth and the 1σ standard deviation were calculated for each clinopyroxenes.

Beneath mid-ocean ridges, liquids can coalesce into small, temporary pockets under permeable barriers such as the lithosphere brittle–ductile boundary (BDB). In our study area, the depth of these potential pockets corresponds to the greatest microseismic activity and crystallisation depths (6–15 km). Assuming the base of the oceanic brittle lithosphere is at the 750 °C isotherm (Phipps Morgan and Chen, 1993), the local thermal model from Ligi *et al.* (2005) predicts a BDB depth of ~10 km. The depths of the pockets, based on both thermobarometry and microseismicity, appear consistent with the estimated depth range of the BDB. These estimated magmatic reservoir depths are greater than those obtained in other part of the MAR (3–4 km; Wanless *et al.*, 2015), which is consistent with the strong cold-edge effect expected close to the Romanche TF.

While microseismicity and crystallisation depths are comparable, these two datasets are snapshots taken at two different times. Clinopyroxenes used for geobarometric calculations were sampled from a lava flow dated at 135.3 ± 11.1 ka. Meanwhile, the microseismicity was recorded by OBSs in 2019. We may hypothesise that the depth of the magma accumulation and differentiation, remained stable over this stretch of time.

Conclusions

We explored in detail a section of the slow-spreading MAR at its eastern intersection with the Romanche TF, combining geological, geochemical, petrological, and geophysical data. The basalts from the studied submersible dive exhibit extreme geochemical variability, almost as large as that of global oceanic basalts. Those variations are coherent with the morphology of the individual volcanic edifices observed in this area. These compositions and their distribution can be related to different eruptive events characterised by specific mantle compositions and melting conditions. The clinopyroxenes present in some K-MORBs recorded mixing events during the magma storage. Furthermore, the crystallisation depths of these clinopyroxenes are consistent with geophysics, suggesting that the depth of the BDB is 10–15 km below the seafloor and has remained stable over 135 kyr.

Acknowledgements

We are grateful to the officers, crew, and scientific party for their hard work during the 2019 SMARTIES cruise onboard the R/V *Pourquoi Pas?*. The ship time for the SMARTIES cruise (Maia *et al.*, 2019; https://doi.org/10.17600/18001107) was granted by the TGIR French Oceanographic Fleet. This work was financially supported by CNRS-INSU Tellus "Campagnes à la mer" and "SYSTER" programs, Région Bretagne and by the ISblue project, Interdisciplinary graduate school for the blue planet (ANR-17-EURE-0015) and co-funded by a grant from the French government under the program "Investissements d'Avenir". We thank the editor, Helen Williams, and Hugh O'Neill, Joshua Shea, and an anonymous reviewer for their constructive comments and suggestions, which greatly improved our manuscript.

Editor: Helen Williams

Additional Information

Supplementary Information accompanies this letter at https://www.geochemicalperspectivesletters.org/article2612.

Cite this letter as: Grenet, L., Hamelin, C., Brunelli, D., Maia, M., Briais, A., Verhoest, L., Yu, Z., Singh, S.C. (2026) The journey of K-MORBs, told through geological, geochemical and geophysical data. *Geochem. Persp. Let.* 39, 48–53. https://doi.org/10.7185/geochemlet.2612

References

Bonatti, E., Ligi, M., Carrara, G., Gasperini, L., Turko, N., Perfiliev, S., Peyve, A., Sciuto, P.F. (1996) Diffuse impact of the Mid-Atlantic Ridge with the Romanche transform: an ultracold ridge-transform intersection. *Journal of Geophysical Research: Solid Earth* 101, 8043–8054. https://doi.org/10.1029/95JB02249

Bonatti, E., Brunelli, D., Fabretti, P., Ligi, M., Asunta Portaro, R., Seyler, M. (2001) Steady-state creation of crust-free lithosphere at cold spots in mid-ocean ridges. *Geology* 29, 979. https://doi.org/10.1130/0091-7613(2001)029<0979:SSCOCF>2.0.CO;2

Brunelli, D., Verhoest, L., Ligi, M., Hemond, C., Maia, M., Soltanmohammadi, A., Lugli, F., Nonnotte, P., Cipriani, A. (2025) Large melt diversity at a mid-ocean ridge thermal low. *Science Advances* 11. https://doi.org/10.1126/sciadv.adv4654

Di Fiore, F., Mollo, S., Vona, A., MacDonald, A., Ubide, T., Nazzari, M., Romano, C., Scarlato, P. (2021) Kinetic partitioning of major and trace cations between clinopyroxene and phonotephritic melt under convective stirring conditions: New insights into clinopyroxene sector zoning and concentric zoning. *Chemical Geology* 584, 120531. https://doi.org/10.1016/j.chemgeo.2021.120531

Grégoire, M., Bell, D., Le Roex, A. (2002) Trace element geochemistry of phlogopite-rich mafic mantle xenoliths: their classification and their relationship to phlogopite-bearing peridotites and kimberlites revisited. *Contributions to Mineralogy and Petrology* 142, 603–625. https://doi.org/10.1007/s00410-001-0315-8

Gregory, E.P.M., Singh, S.C., Marjanović, M., Wang, Z. (2021) Serpentinized peridotite versus thick mafic crust at the Romanche oceanic transform fault. *Geology* 49, 1132–1136. https://doi.org/10.1130/G49097.1

Grenet, L., Maia, M., Hamelin, C., Briais, A., Guillou, H., Scao, V., Brunelli, D. (2025) A Deep Dive Into a Ridge-Transform Fault Intersection: Volcano-Tectonic Relationships in an Enhanced Cold-Edge Effect at the Romanche Fracture Zone. *Journal of Geophysical Research: Solid Earth* 130. https://doi.org/10.1029/2024JB030688

Grevemeyer, I., Hayman, N.W., Lange, D., Peirce, C., Papenberg, C., Van Avendonk, H.J.A., Schmid, F., De La Peña, L.G., Dannowski, A. (2019) Constraining the maximum depth of brittle deformation at slow- and ultra-slow-spreading ridges using microseismicity. *Geology* 47, 1069–1073. https://doi.org/10.1130/G46577.1

Lambart, S. (2017) No direct contribution of recycled crust in Icelandic basalts. *Geochemical Perspectives Letters* 4, 7–12. https://doi.org/10.7185/geochemlet.1728

Le Voyer, M., Cottrell, E., Kelley, K.A., Brounce, M., Hauri, E.H. (2015) The effect of primary versus secondary processes on the volatile content of MORB glasses: An example from the equatorial Mid-Atlantic Ridge (5°N–3°S). *Journal of Geophysical Research: Solid Earth* 120, 125–144. https://doi.org/10.1002/2014JB011160

Leroux, P., Shirey, S., Hauri, E., Perfit, M., Bender, J. (2006) The effects of variable sources, processes and contaminants on the composition of northern EPR MORB (8–10°N and 12–14°N): Evidence from volatiles (H2O, CO2, S) and halogens (F, Cl). *Earth and Planetary Science Letters* 251, 209–231. https://doi.org/10.1016/j.epsl.2006.09.012

Ligi, M., Bonatti, E., Cipriani, A., Ottolini, L. (2005) Water-rich basalts at mid-ocean-ridge cold spots. *Nature* 434, 66–69. https://doi.org/10.1038/nature03264

MacDonald, A., Ubide, T., Mollo, S. (2024) Degree of sector zoning in clinopyroxene records dynamic magma recharge and ascent. *Geochimica et Cosmochimica Acta* 378, 245–258. https://doi.org/10.1016/j.gca.2024.06.025

Maia, M., Brunelli, D., Ligi, M. (2019) SMARTIES cruise, RV Pourquoi pas ? https://doi.org/10.17600/18001107

Mollo, S., Putirka, K., Misiti, V., Soligo, M., Scarlato, P. (2013) A new test for equilibrium based on clinopyroxene–melt pairs: Clues on the solidification temperatures of Etnean alkaline melts at post-eruptive conditions. *Chemical Geology* 352, 92–100. https://doi.org/10.1016/j.chemgeo.2013.05.026

Neave, D.A., Putirka, K.D. (2017) A new clinopyroxene-liquid barometer, and implications for magma storage pressures under Icelandic rift zones. *American Mineralogist* 102, 777–794. https://doi.org/10.2138/am-2017-5968

Petrone, C.M., Mollo, S., Gertisser, R., Buret, Y., Scarlato, P., Del Bello, E., Andronico, D., Ellis, B., Pontesilli, A., De Astis, G., Giacomoni, P.P., Coltorti, M., Reagan, M. (2022) Magma recharge and mush rejuvenation drive paroxysmal activity at Stromboli volcano. *Nature Communications* 13, 7717. https://doi.org/10.1038/s41467-022-35405-z

Phipps Morgan, J., Chen, Y.J. (1993) Dependence of ridge-axis morphology on magma supply and spreading rate. *Nature* 364, 706–708. https://doi.org/10.1038/364706a0

Putirka, K.D. (2008) Thermometers and Barometers for Volcanic Systems. *Reviews in Mineralogy and Geochemistry* 69, 61–120. https://doi.org/10.2138/rmg.2008.69.3

Schilling, J.-G., Hanan, B.B., McCully, B., Kingsley, R.H., Fontignie, D. (1994) Influence of the Sierra Leone mantle plume on the equatorial Mid-Atlantic Ridge: A Nd-Sr-Pb isotopic study. *Journal of Geophysical Research: Solid Earth* 99, 12005–12028. https://doi.org/10.1029/94JB00337

Schilling, J.-G., Ruppel, C., Davis, A.N., McCully, B., Tighe, S.A., Kingsley, R.H., Lin, J. (1995) Thermal structure of the mantle beneath the equatorial Mid-Atlantic Ridge: Inferences from the spatial variation of dredged basalt glass compositions. *Journal of Geophysical Research* 100, 10057–10076. https://doi.org/10.1029/95JB00668

Shaw, D.M. (2000) CONTINUOUS (DYNAMIC) MELTING THEORY REVISITED. *The Canadian Mineralogist* 38, 1041–1063. https://doi.org/10.2113/gscanmin.38.5.1041

Ubide, T., Mollo, S., Zhao, J., Nazzari, M., Scarlato, P. (2019) Sector-zoned clinopyroxene as a recorder of magma history, eruption triggers, and ascent rates. *Geochimica et Cosmochimica Acta* 251, 265–283. https://doi.org/10.1016/j.gca.2019.02.021

Verhoest, L. (2022) Melting a heterogeneous Earth's mantle under an extreme thermal gradient. Doctoral dissertation, Université de Bretagne occidentale-Brest; Università degli studi di Modena e Reggio Emilia. https://theses.hal.science/tel-05351687

Wanless, V.D., Shaw, A.M., Behn, M.D., Soule, S.A., Escartín, J., Hamelin, C. (2015) Magmatic plumbing at Lucky Strike volcano based on olivine-hosted melt inclusion compositions. *Geochemistry, Geophysics, Geosystems* 16, 126–147. https://doi.org/10.1002/2014GC005517

Wieser, P.E., Kent, A.J.R., Till, C.B. (2023a) Barometers Behaving Badly II: a Critical Evaluation of Cpx-Only and Cpx-Liq Thermobarometry in Variably-Hydrous Arc Magmas. *Journal of Petrology* 64, egad050. https://doi.org/10.1093/petrology/egad050

Wieser, P.E., Kent, A.J.R., Till, C.B., Donovan, J., Neave, D.A., Blatter, D.L., Krawczynski, M.J. (2023b) Barometers Behaving Badly I: Assessing the Influence of Analytical and Experimental Uncertainty on Clinopyroxene Thermobarometry Calculations at Crustal Conditions. *Journal of Petrology* 64, egac126. https://doi.org/10.31223/X5JT0N

Workman, R.K., Hart, S.R. (2005) Major and trace element composition of the depleted MORB mantle (DMM). *Earth and Planetary Science Letters* 231, 53–72. https://doi.org/10.1016/j.epsl.2004.12.005

Yu, Z., Singh, S.C., Hamelin, C., Grenet, L., Maia, M., Briais, A., Petracchini, L., Brunelli, D. (2025) Deep mantle earthquakes linked to CO_2 degassing at the mid-Atlantic ridge. *Nature Communications* 16, 563. https://doi.org/10.1038/s41467-024-55792-9

Zhou, J.-S., Wang, Q., Xing, C.-M., Ma, L., Hao, L.-L., Li, Q.-W., Wang, Z.-L., Huang, T.-Y. (2021) Crystal growth of clinopyroxene in mafic alkaline magmas. *Earth and Planetary Science Letters* 568, 117005. https://doi.org/10.1016/j.epsl.2021.117005

Geochemical Perspectives Letters

The journey of K-MORBs, told through geological, geochemical and geophysical data

L. Grenet, C. Hamelin, D. Brunelli, M. Maia, A. Briais, L. Verhoest, Z. Yu, S.C. Singh

Supplementary Information

The Supplementary Information includes:

- 1. Whole Rock: Major and Trace Elements
- 2. Minerals: Major and Trace Element Analysis and Imaging
- 3. Pyroxenes Thermobarometry and Hygrometer Calculations
- 4. Description of Samples
- Figures S-1 to S-18
- Table S-1
- Tables S-2 to S-20 (.xlsx)
- Supplementary Information References

1. Whole Rock: Major and Trace Elements

Major and trace elements of the groundmass were measured at the PSO/IUEM (Pôle Spectrométrie Océan, Institut Universitaire Européen de la Mer, Brest, France). For major element analysis, samples were crushed and sieved, the size fraction of 2-1 mm was retained. Phenocrysts and fractions with alteration were manually removed. A mass of 250 mg of the 2-1 mm fraction was dissolved in closed screw-top Teflon vessels (Savillex), at about 90 °C for 24h using 1 ml of HNO_3 and 3 ml of HF. Then 96 ml of H_3BO_3 were added to neutralise the effect of HF (Cotten *et al.*, 1995). Major element compositions were measured by an inductively coupled plasma-atomic emission spectrometer (ICP-AES) using Horiba Jobin Yvon® Ultima 2. Calibrations were made using international standards JB2, ACE, ME, and WSE, and internal standards CB2, BELC, CB15 and CB18.

Trace elements were analysed with a high-resolution inductively coupled plasma mass spectrometer (HR-ICPMS) ELEMENT XR, ThermoFisher Scientific. Samples were prepared following Barrat *et al.* (1996) protocol. Powdered samples (100 mg) were dissolved in screw-top Teflon vessels (Savillex) using an HF-HNO_3 mixture and evaporated to dryness. Dry residues were then dissolved in 40 g of 6N HCl. An aliquot of 1 ml of this solution was collected; a solution of pure Tm was added and then evaporated to dryness. Samples were taken up in 2.5 % HNO_3 for analysis on the ICP-MS. Calibrations were made using BCR2 and WSE standards.

2. Minerals: Major and Trace Element Analysis and Imaging

Major element compositions were determined by electron probe microanalysis (EPMA), using a Cameca SX100 electron microprobe (Microsonde Ouest, Brest, France). Analyses were performed on carbon-coated polished thin sections under the following conditions: 15 kV accelerating voltage, 20 nA beam current, spot size of 1 µm and 10 s (20 s for F and 30 s for Ti) counting time on the peak. Standards were natural albite (Na), forsterite (Mg), apatite (F, P), wollastonite (Si, Ca), corundum (Al), orthoclase (K), $MnTiO_3$ (Ti, Mn), andradite (Fe), pyromorphite (Cl), Cr_2O_3 (Cr), and NiO (Ni). Electron microprobe transects were performed on clinopyroxene phenocrysts, each spot separated by 10 µm (for small crystals and transversal profiles) to 20 µm (for longitudinal profiles). The error in an analysis is considered to be 1 % of the value. For mapping, we used 1 to 2 µm pixel size and 100 s dwell time per pixel, measuring nine to ten elements per map. The size of maps varies from 253 x 253 µm to 1428 x 2023 µm.

The target minerals for trace element analysis were chosen by combining microscope observations and scanning electron microscope (SEM). Thick section imaging was carried out using JEOL JSM-6010LA InTouchScope SEM at 20 kV in the Dipartimento di Scienze Chimiche e Geologiche of Modena (Italy).

The trace elements were measured on clinopyroxene phenocrysts. They were measured by laser ablation inductively coupled mass spectrometer (LA-ICP-MS) at Centro Interdipartimentale Grandi Strumenti (CIGS, Modena), using Thermo Scientific iCAP TQ ICP-MS. Analyses were performed on 90 µm-thick polished thin sections. Analyses were run over 30 s, using 100 % energy output, a 10 Hz repeat rate, and a 55 µm spot size. Three standards (NIST 612, NIST 614 and MLB3) were analysed at the beginning and end of each session. Data were normalised with the SiO_2 of each crystal as an internal standard obtained by averaging three analyses realised by EPMA. The number of crystal targets was limited by the size of the minerals, which must be larger than 55 µm. Areas of analysis must be flat, without fracture or inclusion to avoid diffusive effects and uniquely measure the mineral composition. When the conditions were met, we performed at least two points of analysis, one in the centre and one in the rim to investigate if the composition of the crystals varies during their crystallisation.

3. Pyroxene Thermobarometry Calculations

Thermobarometric calculations using the clinopyroxene major compositions, from thin section analysis, were performed using an iterative approach adapted from Neave and Putirka (2017). The temperature was estimated using Equation 33 from Putirka (2008), this model has a standard estimated error (SEE) of 45 °C. The pressure was estimated using Neave

and Putirka (2017) model, adapted to alkaline hydrated lavas and independent of the water content. This model has a SEE of 1.4 kbar.

Temperature and pressure of crystallisation were calculated for clinopyroxenes using in situ analyses and profiles. The equilibrium between the clinopyroxenes and the whole rock was estimated by calculating the $K_D(Fe–Mg)_{cpx–liq}$ from the whole rock with Equation 35 of Putirka (2008). We consider that, the equilibrium was reached for a $K_D = 0.03 \pm 0.08$ (Wieser *et al.*, 2023). Diopside-Hedenbergite (DiHd), Enstatite-Ferrosilite (EnFs), and Calcium-Tschermak (CaTs) component equilibria were tested using Mollo *et al.* (2013) (for DiHd and EnFs) and Putirka (1999) (for CaTs). We used thresholds of 0.06, 0.05, and 0.03 for the ΔDiHd, ΔEnFs, and ΔCaTs components, respectively, corresponding to the SEE reported by Mollo *et al.* (2013). Only the clinopyroxene-whole rock pairs, which present equilibrium for all tested parameters, were kept and considered as meaningful for P-T petrological interpretations. The clinopyroxenes are sector zoned; one zone is Si-Mg-rich, and the other is Al-Ti-rich. According to Zhou *et al.* (2021), in sector-zoned clinopyroxenes, the SiO_2-rich sectors are closer to real equilibrium than Al_2O_3-rich sectors. Hence, only analyses realised in Si-Mg-rich sectors are kept for P-T.

4. Description of Samples

Seamount

The samples collected from the seamount are sparsely plagioclase-phyric basalts with a microlithic groundmass dominated by plagioclase with olivine. They are moderately fresh, with few vesicles. Those samples are characterised by phenocrysts of plagioclases euhedral to subhedral. Some phenocrysts have sieve texture with external resorption. They frequently have elongated or small circular inclusions. Numerous microphenocrysts are present, they have an acicular or skeletal shape. Olivine phenocrysts are rare and are subhedral to skeletal. Most olivine crystals are subhedral to skeletal microphenocrysts, forming glomerophyres with plagioclases.

Cone

The samples collected from the cone (SMA1974-278 and SMA1974-279), are porphyric alkaline basalts, dominated by clinopyroxene phenocrysts with olivine phenocrysts often organised as glomerophyres (Fig. S-8). Both samples are moderately fresh and vesicular. Clinopyroxene phenocrysts are euhedral to subhedral. They are sector-zoned and have oscillatory zoning. Olivine phenocrysts are mostly skeletal, the smallest are subhedral.

The groundmass is different between both samples. The groundmass of SMA1974-278 is glassy with clinopyroxene microliths, while the groundmass of SMA1974-279 is almost entirely crystallised and composed by microliths of clinopyroxene and plagioclase (Fig.S-8 c, d). In both samples, microliths of amphibole and biotite are present around vesicles or between glomerocrysts (Fig. S-8 e, f). Amphiboles are frequently found in small patches within the matrix of SMA1974-278 and sometimes as small needles growing on the surface of larger clinopyroxenes. They have a rhombus-shape. Microliths of biotite are present as small needles.

Narrow ridge

The samples from the narrow ridge are aphyric basalts. They are moderately fresh; some cracks and vesicles are filled by iron hydroxides. Phenocrysts of plagioclase and olivine are almost absent and are sometimes present as glomerophyres. The groundmass is microlithic, composed by plagioclases, without clear foliation. Plagioclase microphenocryts are acicular or skeletal and olivines are subhedral to skeletal.

Axial volcanic ridge

The samples from the axial volcanic ridge are an aphyric basalts. The sample are moderately fresh; some cracks are filled by iron hydroxides. Microphenocrysts of plagioclase and olivine are numerous, while phenocrysts are almost absent. The groundmass is microlithic, composed by plagioclases, without clear foliation. Plagioclase microphenocrysts are acicular or skeletal and olivines are subhedral to skeletal. Glomerophyres of plagioclases and olivines are frequent.

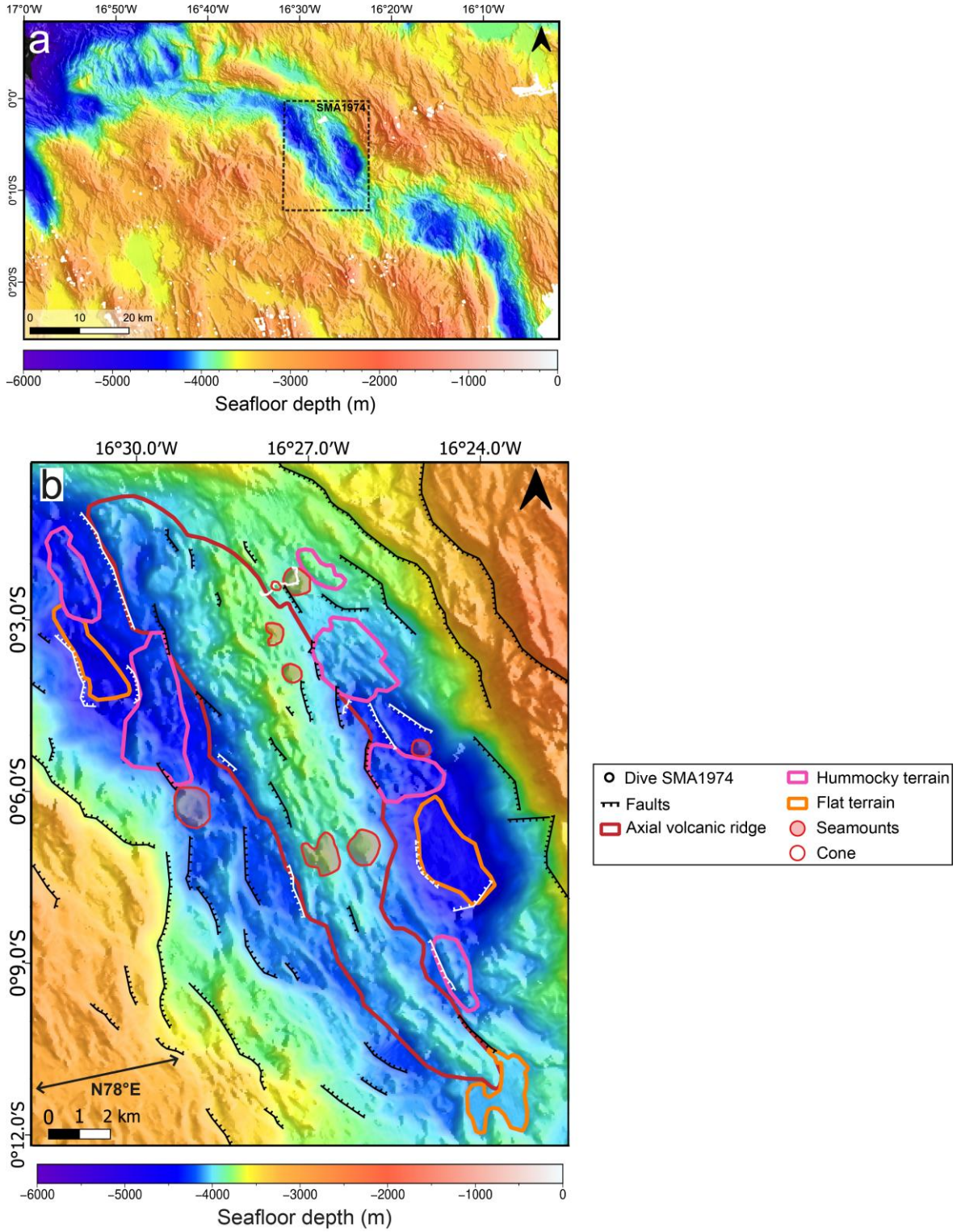

Figure S-1 Bathymetric and structural maps. **(a)** Bathymetric map, combining swath bathymetry collected during the SMARTIES cruise and previous cruises. The black dashed rectangle outlines the segment RC2. **(b)** Main volcano-tectonic features of segment RC2 reported on the bathymetric map, including the axial volcanic ridge (red line), hummocky (pink line) and flat (orange line) volcanic terrains, seamounts (brownish surfaces), the cone explored during dive SMA1974, and faults. Modified from Grenet *et al.* (2025).

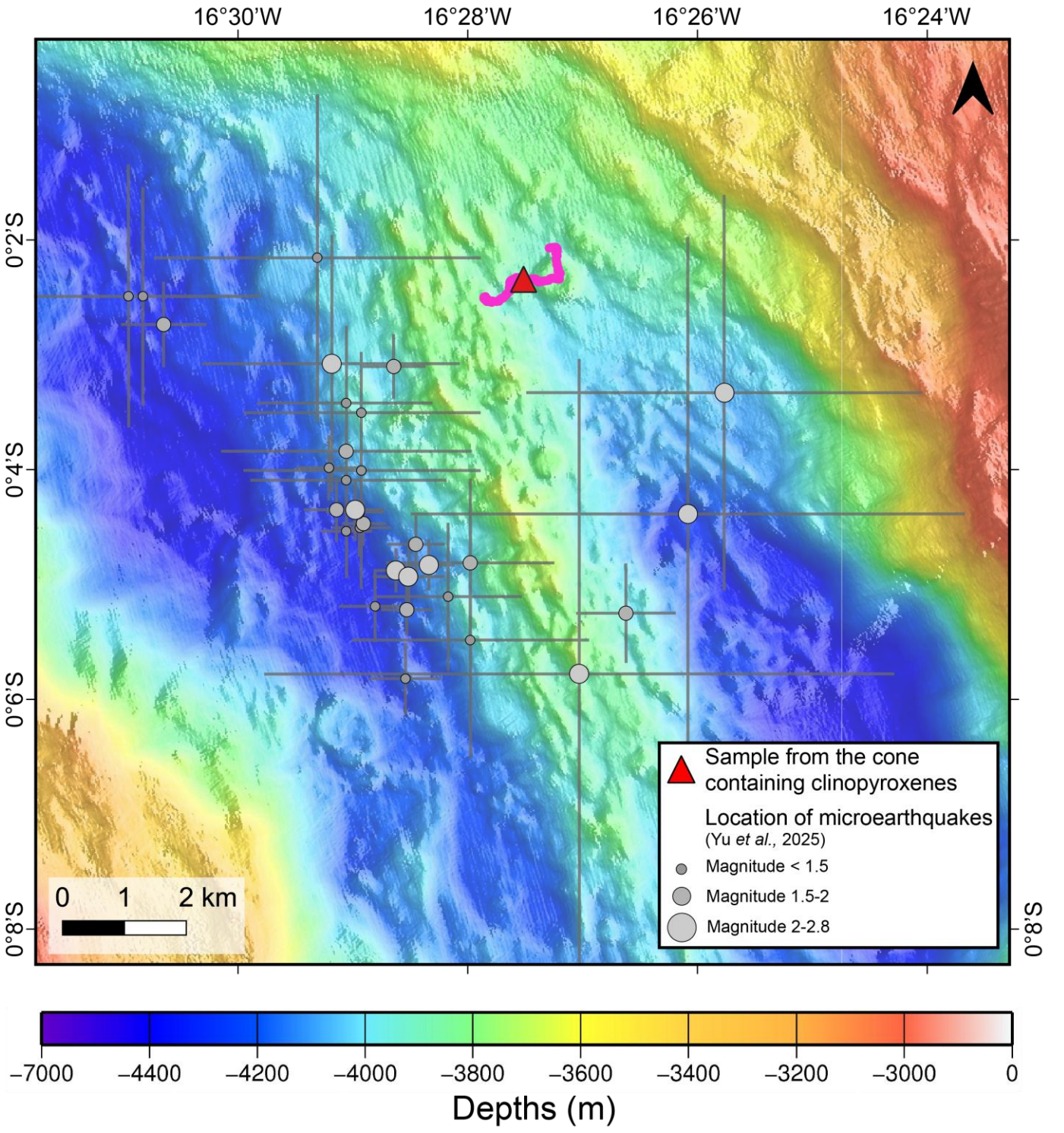

Figure S-2 Bathymetric map of the segment RC2 with the locations of the dive SMA1974 (pink track), the samples containing the studied clinopyroxenes, and the microearthquakes from Yu *et al*. (2025). The location error is represented by the lines.

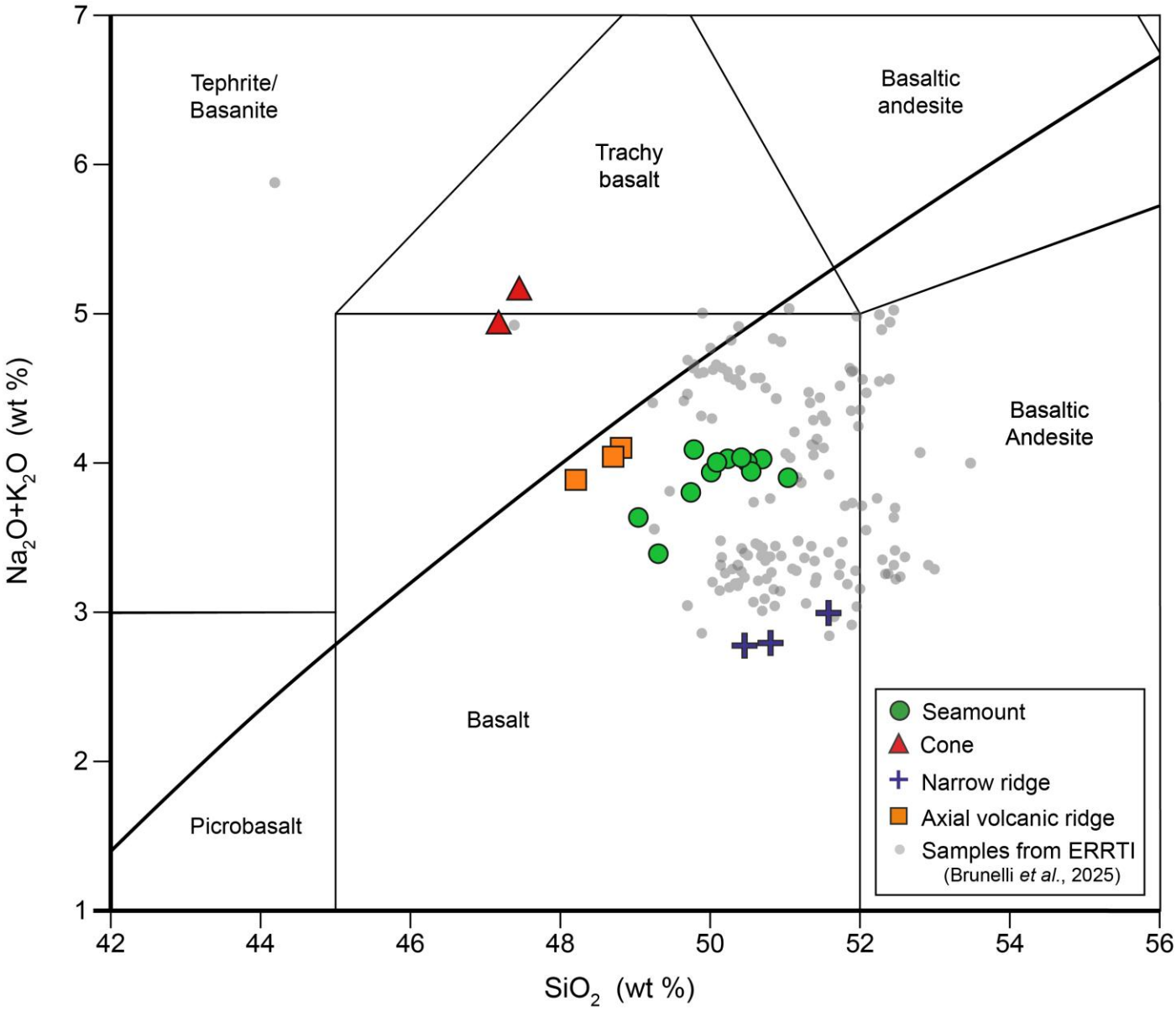

Figure S-3 Basaltic glass and whole rock compositions of the ERRTI samples collected during SMARTIES cruise. Total alkali *versus* silica (wt. %). Seamount and AVR data are from Brunelli *et al.* (2025).

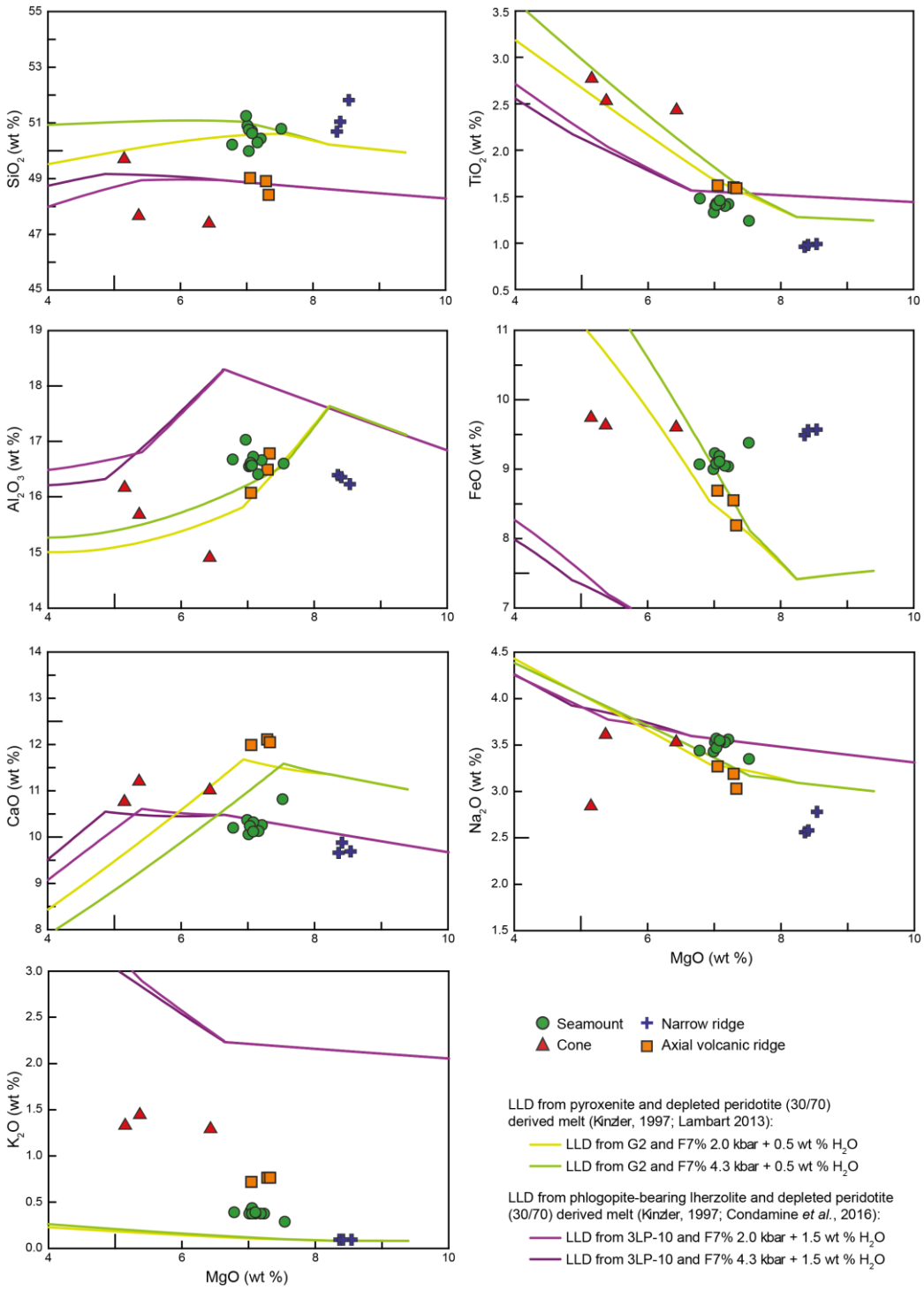

Figure S-4 Major element composition *vs.* MgO of basaltic glass and whole rock compositions of the samples collected during the dive SMA1974. Calculated LLD calculated with Petrolog3 using Danyushevsky and Plechov (2011) from mixing between a depleted peridotite and various sources: light green and green are a mixing between 70 % of aggregated melt at average melting of 7 % of a depleted peridotite (Kinzler, 1997) with 30 % melt from partial melting of eclogite G2 (Lambart, 2017); light and dark purple are a mixing between 70 % of aggregated melt at average melting of 7 % of a depleted peridotite (Kinzler, 1997) with 30 % melt from partial melting of a phlogopite-bearing lherzolite (3LP-10) (Condamine *et al.*, 2016).

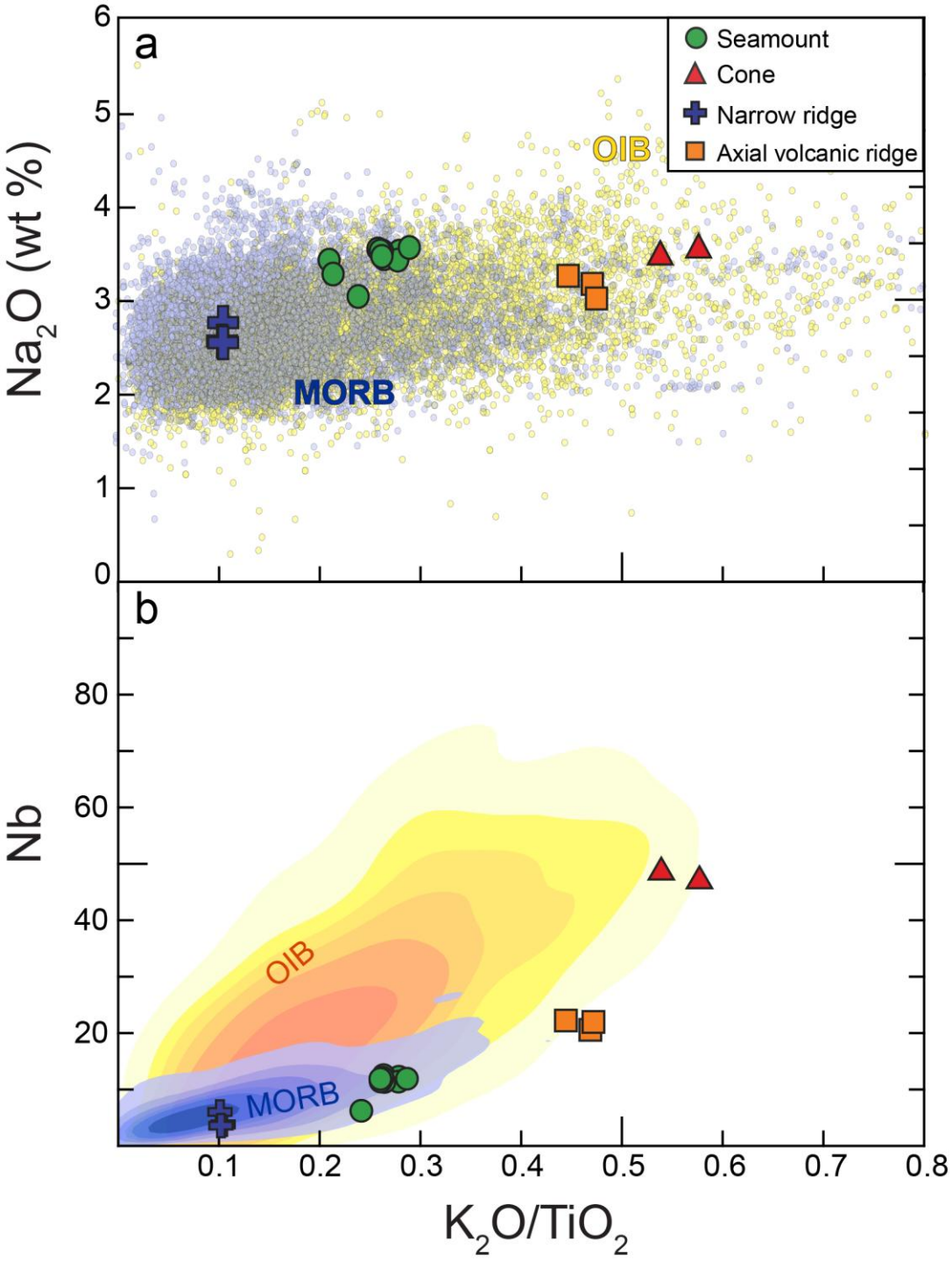

Figure S-5 Plots of Na_2O **(a)** and Nb (in ppm) **(b)** versus K_2O/TiO_2 for samples from dive SMA1974. The mid-oceanic ridge basalts (MORB) and ocean island basalts (OIB) fields represent the distribution of the composition of oceanic basalts from global data sets. In **(a)** there are 22,183 samples from PetDB for MORBs and 8,535 samples from GEOROC for OIBs. In **(b)** there are 9,289 samples for MORBs and 5,251 samples for OIBs, both from GEOROC. The different fields correspond to proportions of the sample population from the darkest colours to the lightest: 30 %; 50 %; 60 %; 70 %; 80 % and 90 %.

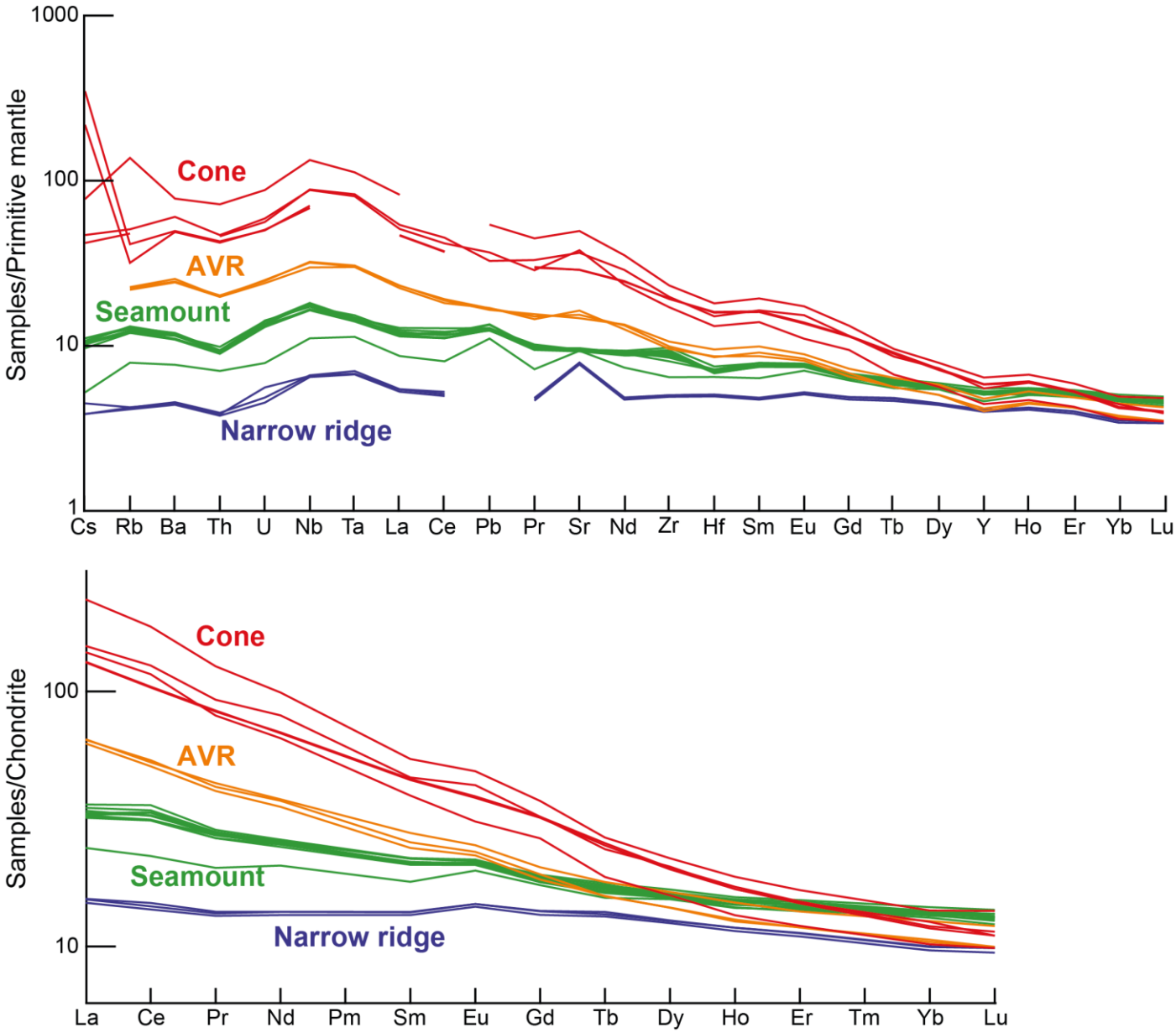

Figure S-6 Extended trace element patterns normalised to Primitive Mantle (Sun and McDonough, 1989) and REE normalised to chondrite (Sun and McDonough, 1989) of basaltic glass and whole rock trace compositions of the samples collected during the dive SMA1974. Seamount and AVR data are from Brunelli *et al*. (2025).

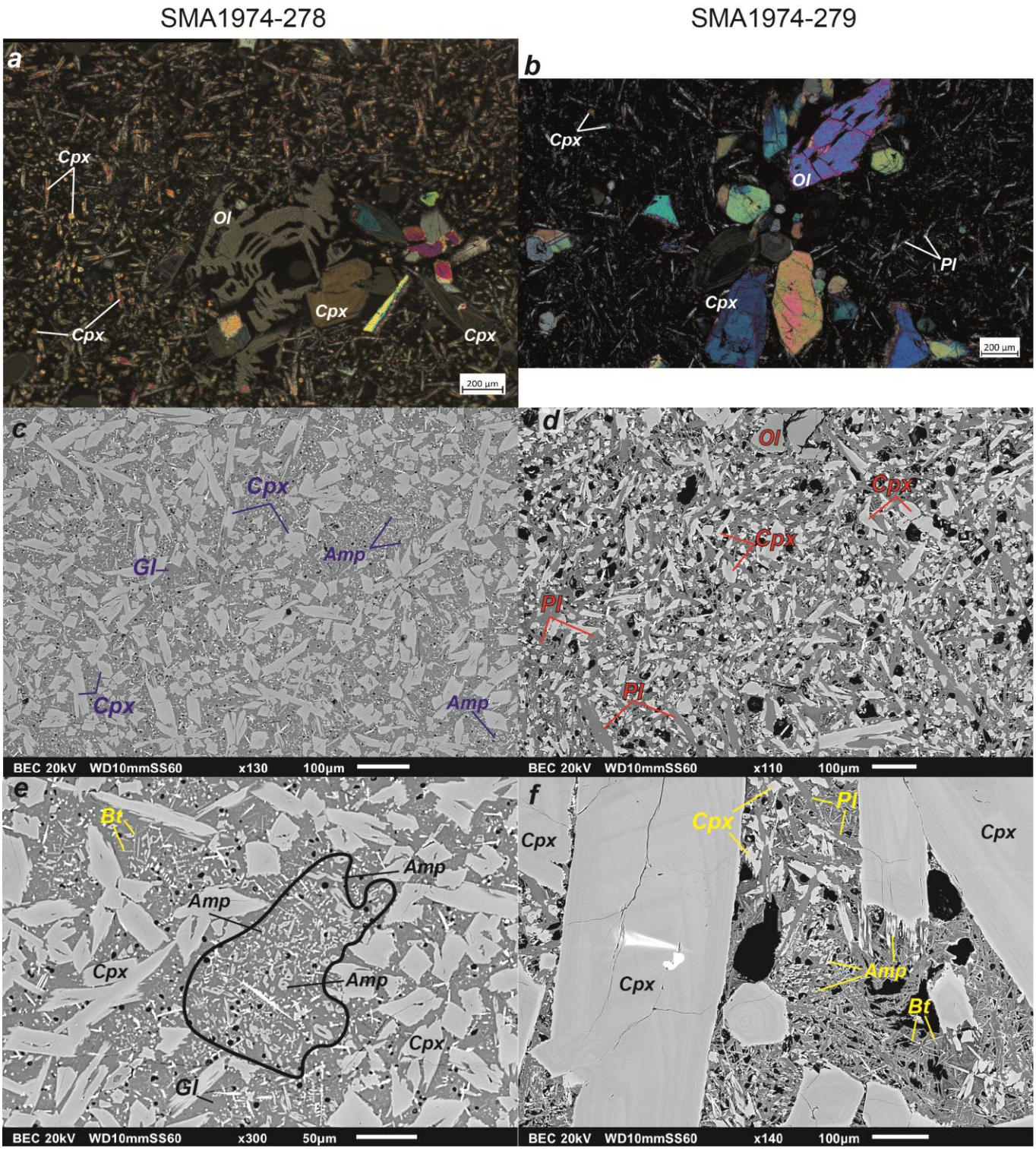

Figure S-8 Images of sample SMA1974-278 on the left of the plate (a. c. e. g) and of sample SMA1974-279 on the right (b. d. f). Microscope images in cross-polarised light (a-b) and Backscatter Scanning Electron Microscope images (c-g). **(a)** Glomerophyre composed of phenocrysts of skeletal and small olivines and zoned clinopyroxenes. The groundmass is mainly composed of microliths of clinopyroxene. **(b)** Glomerophyre composed of phenocrysts of skeletal and small olivines and zoned clinopyroxenes. The groundmass is composed of microliths of clinopyroxenes and plagioclases. **(c)** Glassy groundmass with numerous microliths of clinopyroxenes and microliths of amphiboles. **(d)**

Microcrystalline groundmass composed of microliths of clinopyroxenes and plagioclases. The black zones are vesicles. **(e)** The black line delimits a group of amphiboles characterized by their rhombus-shape. Some needles are visible in the glass, which are possibly biotites. **(f)** Numerous small biotites are presented, located between phenocrysts of clinopyroxenes; grouped amphiboles are also present, some seem to be in the extension of a clinopyroxene.

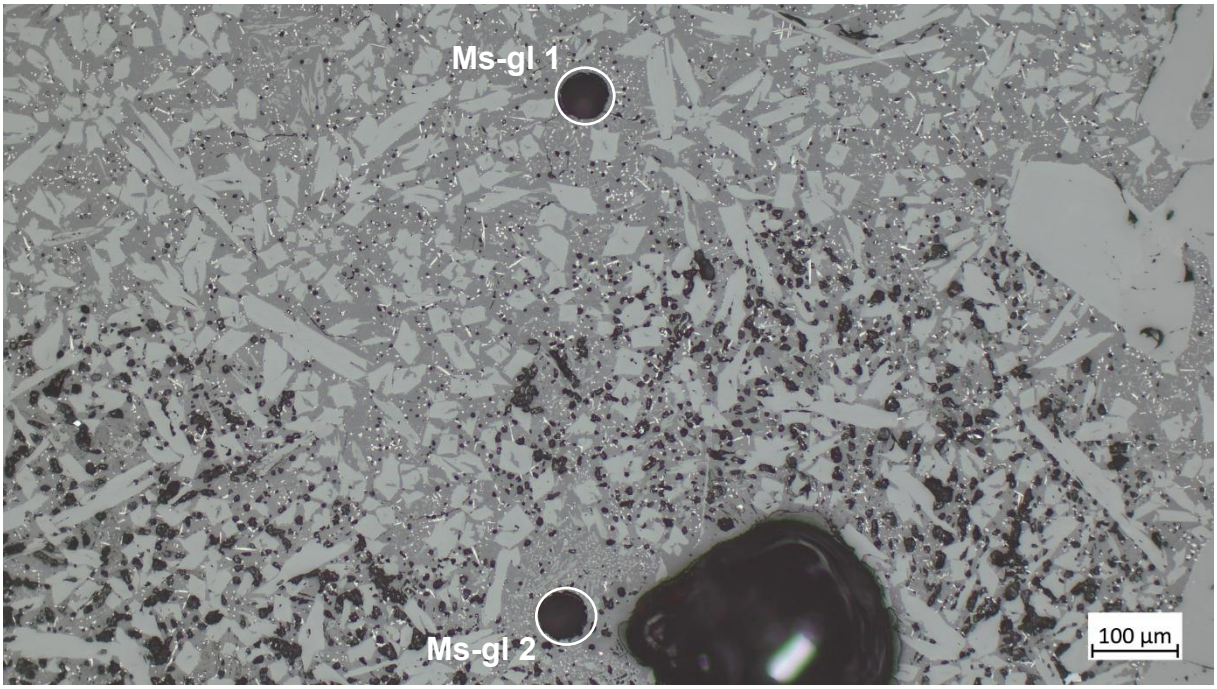

Figure S-9 Laser points of mesostasis glass (Ms-gl) 1 and 2 from sample SMA1974-278.

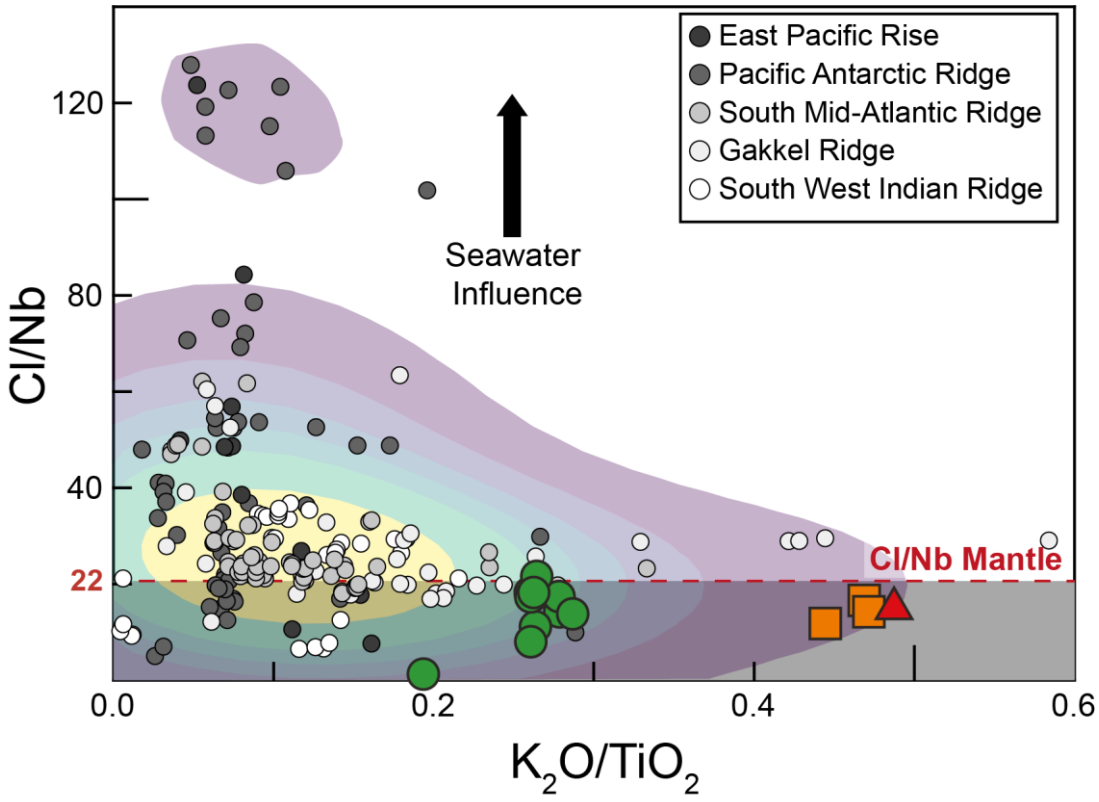

Figure S-10 Volatiles and incompatible elements versus K_2O/TiO_2 ratio for samples from dive SMA1974 and for fast to ultra-slow spreading ridges: East Pacific ridge (9-14°) (Marschall *et al.*, 2017); East Pacific ridge Siqueiros (Marschall *et al.*, 2017); southern Mid-Atlantic Ridge (Van Der Zwan *et al.*, 2017); Gakkel ridge (Van Der Zwan *et al.*, 2017) and Southwest Indian ridge (Kendrick *et al.*, 2017; Marschall *et al.*, 2017; Wang *et al.*, 2021). The Cl/Nb mantle ratio is from Van der Zwan *et al.* (2017).

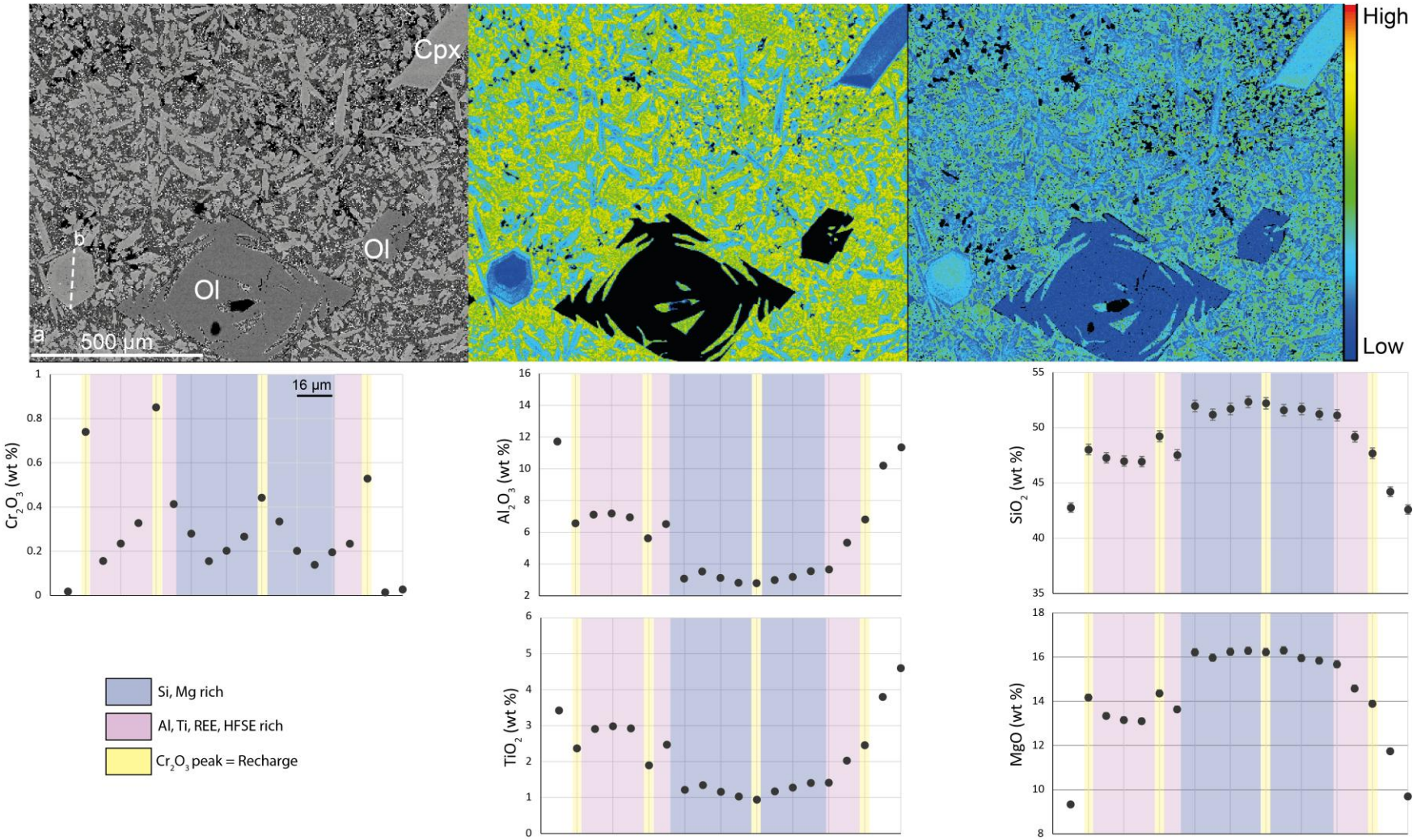

Figure S-11 Sample SMA1974-278. Backscatter electron (BSE) image and major element maps (Al and Si) of olivine and diopside phenocrysts obtained by electron microprobe. The dashed line marks the trace of the profile analysis. Electron microprobe profiles of Cr_2O_3, Al_2O_3, SiO_2, TiO_2 and MgO contents along a-b profile. Measurements at 10 µm step. The error bar represents 1 % of the value obtained; it is included in the symbol for Cr_2O_3, Al_2O_3 and TiO_2. The dark purple area represents Si-Mg-rich sector, the pink the Al-Ti-rich sector and the white zones is the outermost rim. Peaks in Cr_2O_3 are present in yellow on the profile. Cpx: clinopyroxene; Ol: olivine.

Table S-1 Non-modal batch melting aggregated melt calculated for trace element modelling.

	Starting composition	Mineral abundance	Melting mode	Partition coefficient	Mixing
D-DMM spinel	D-DMM (Workman and Hart, 2005)	0.53 Ol + 0.27 Opx + 0.17 Cpx + 0.03 Sp (Hellebrand, 2002)	-0.06 Ol + 0.28 Opx + 0.67 Cpx + 0.11 Sp (Hellebrand *et al.*, 2002)	Duvernay *et al.*, (2024)	
D-DMM garnet	D-DMM (Workmann *et al.*, 2005)	0.57 Ol + 0.21 Opx + 0.13 Cpx + 0.09 Gt (Hellebrand *et al.*, 2002)	0.04 Ol - 0.19 Opx + 1.05 Cpx + 0.11 Gt (Hellebrand *et al.*, 2002)	Duvernay *et al.*, (2024)	
E-DMM spinel	E-DMM (Workmann *et al.*, 2005)	0.53 Ol + 0.27 Opx + 0.17 Cpx + 0.03 Sp (Hellebrand *et al.*, 2002)	-0.06 Ol + 0.28 Opx + 0.67 Cpx + 0.11 Sp (Hellebrand *et al.*, 2002)	Duvernay *et al.*, (2024)	
E-DMM garnet	E-DMM (Workmann *et al.*, 2005)	0.57 Ol + 0.21 Opx + 0.13 Cpx + 0.09 Gt (Hellebrand *et al.*, 2002)	0.04 Ol - 0.19 Opx + 1.05 Cpx + 0.11 Gt (Hellebrand *et al.*, 2002)	Duvernay *et al.*, (2024)	
D-DMM + pyroxenite	Recycled oceanic crust, G2 (Lambart, 2017)	0.75 Cpx + 0.25 Grt (Pertermann *et al.*, 2004)	-0.51 Ol + 0.86 Opx + 0.57 Cpx + 0.11 Gt (Borghini *et al.*, 2017)	Pertermann *et al.*, (2004)	1 % F Sp-D-DMM; 1 % F Gt-D-DMM; 4 % F G2
D-DMM + phlogopite	Phlogopite-bearing lherzolite source, BD 2348 PP lherzolite (Grégoire *et al.*, 2002)	0.67 Ol + 0.29 Opx + 0.01 Cpx + 0.01 Sp + 0.03 Phl (Grégoire *et al.*, 2002)	-0.58 Ol + 0.56 Opx + 0.47 Cpx + 0.05 Sp + 0.49 Phl (Condamine and Médard, 2014)	Condamine *et al.*, (2022)	1 % F Sp-D-DMM and 1 % F Gt-D-DMM; 4 % F BD 2348 PP

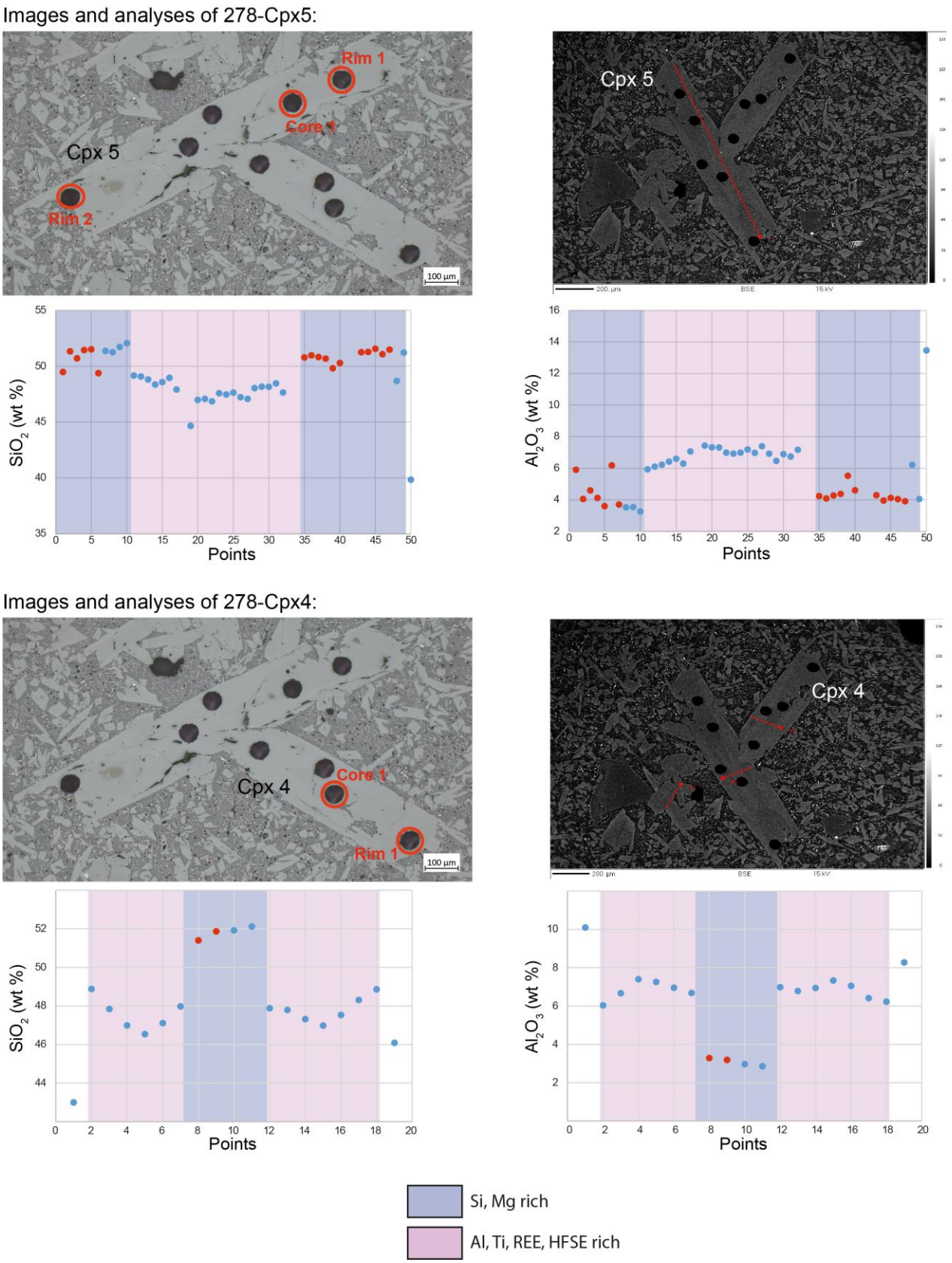

Figure S-13 BSE images and analysis profiles of Cpx5 and Cpx4 from SMA1974-278 used for geothermobarometric calculations. The red dots on the profiles are the points used for the geothermobarometric calculations (see Table S-20).

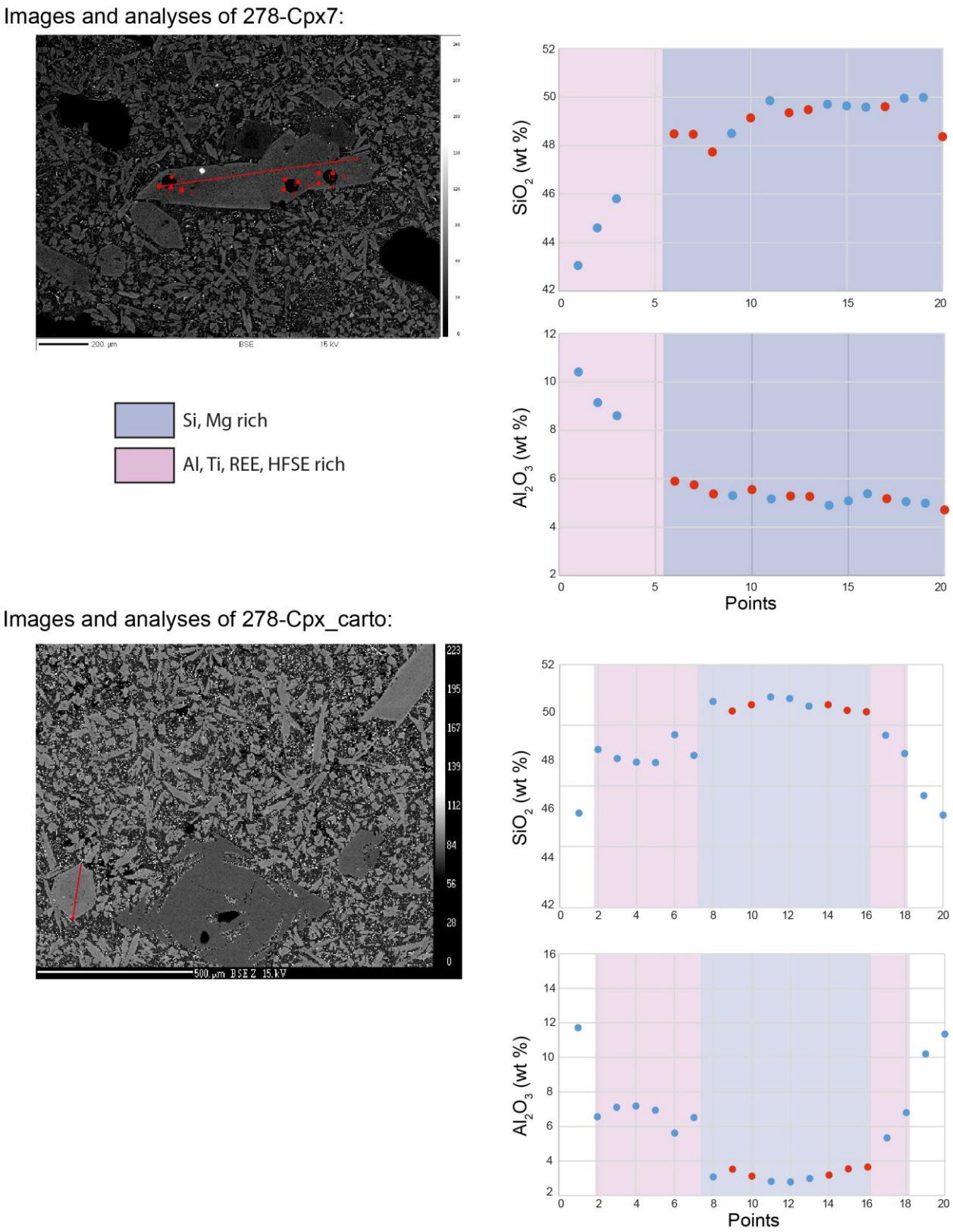

Figure S-14 BSE images and analysis profiles of Cpx7 and Cpx_carto from SMA1974-278 used for geothermobarometric calculations. The red dots on the profiles are the points used for the geothermobarometric calculations (see Table S-20).

Images and analyses of 278-Cpx_5-4:

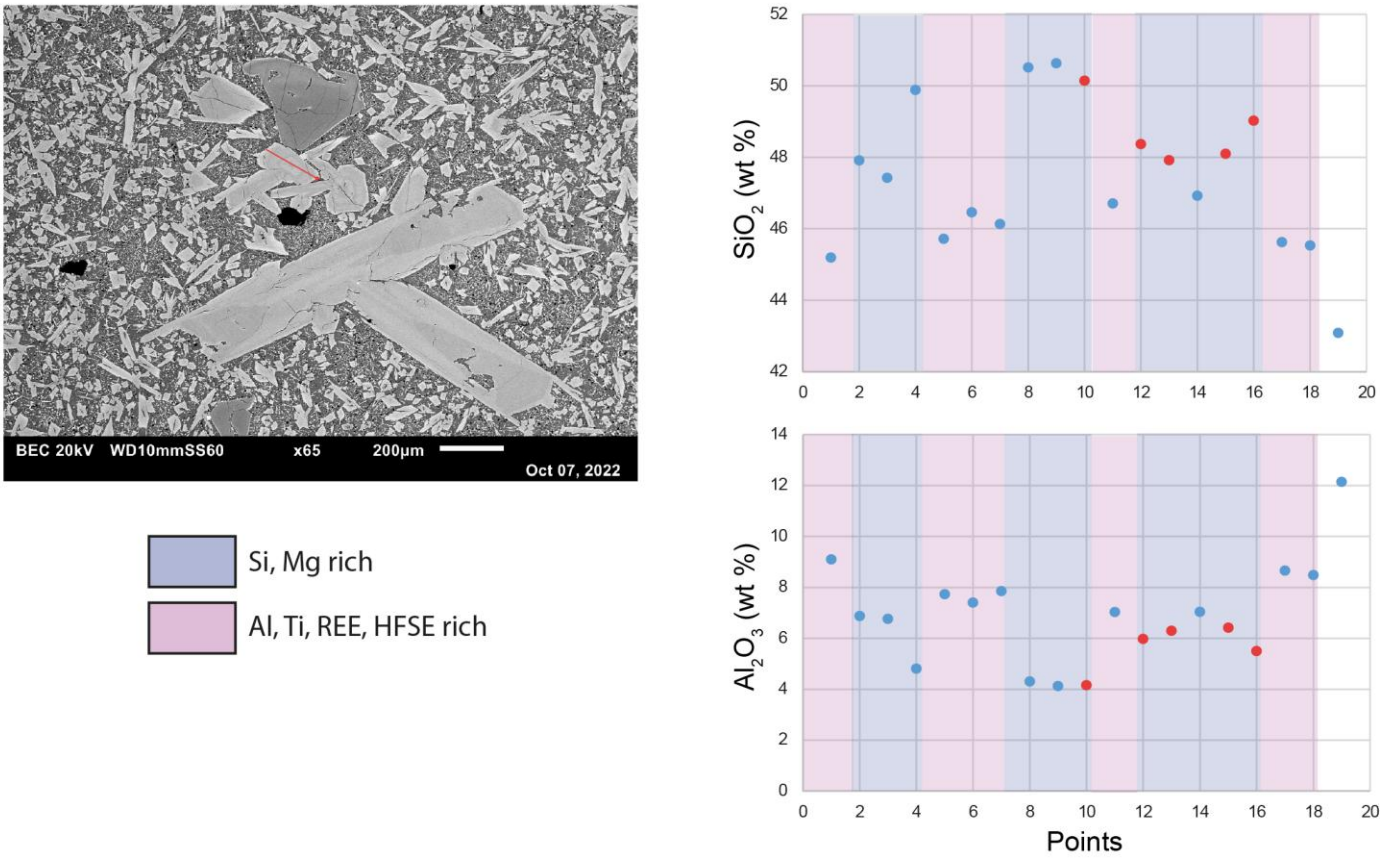

Figure S-15 BSE images and analysis profiles of Cpx5-4 from SMA1974-278 used for geothermobarometric calculations. The red dots on the profiles are the points used for the geothermobarometric calculations (see Table S-20).

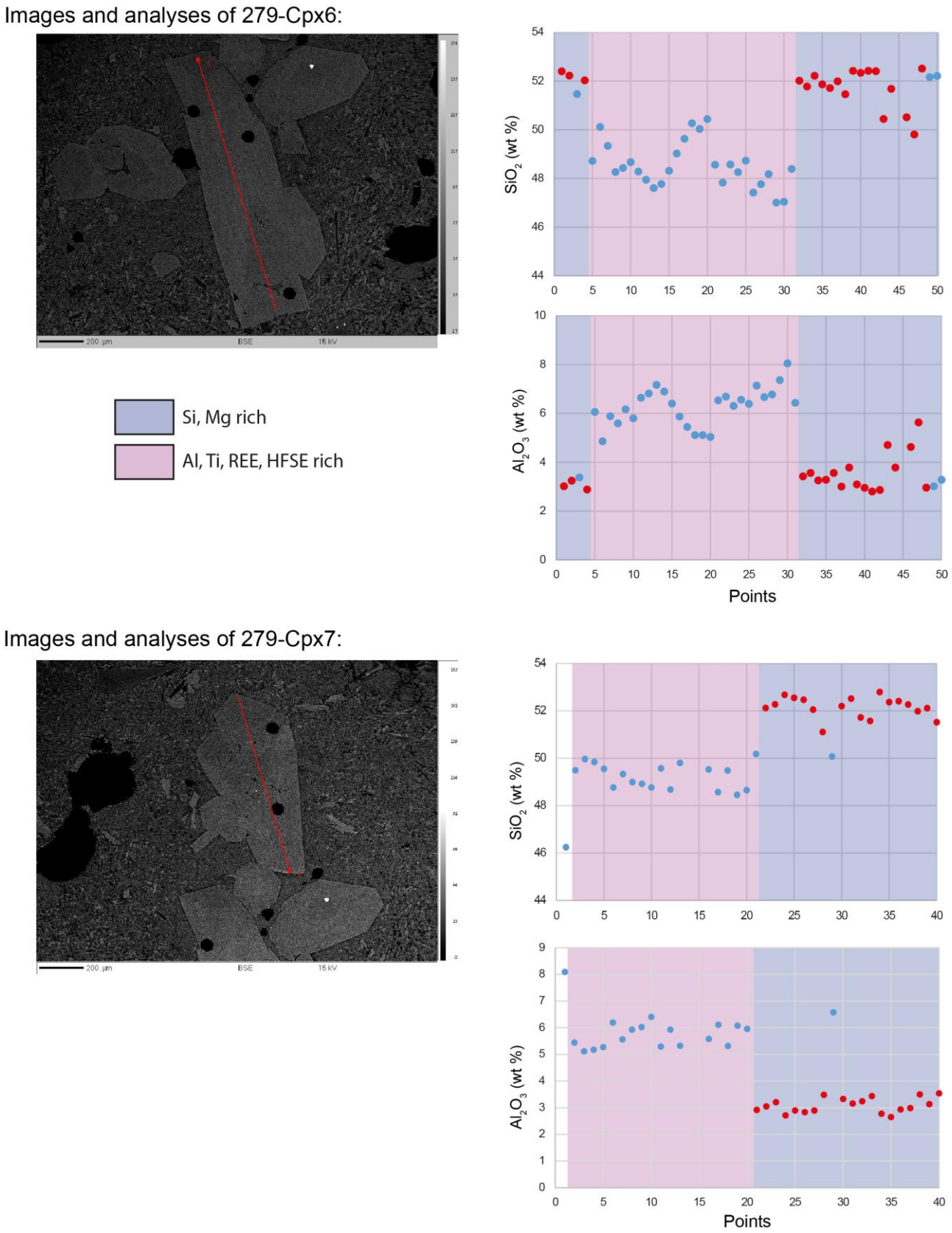

Figure S-16 BSE images and analysis profiles of Cpx6 and Cpx7 from SMA1974-279 used for geothermobarometric calculations. The red dots on the profiles are the points used for the geothermobarometric calculations (see Table S-20).

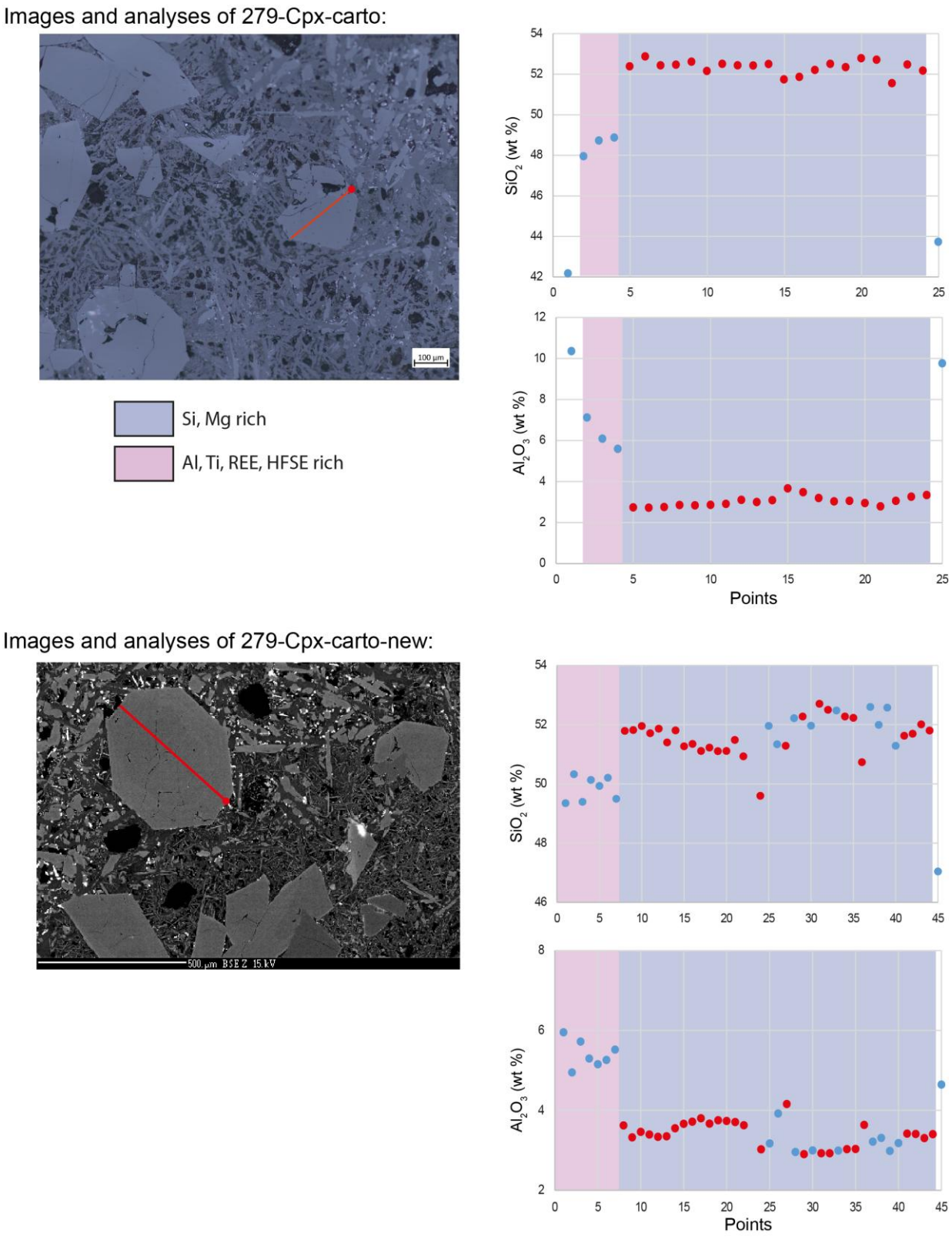

Figure S-17 BSE images and analysis profiles of Cpx-carto and Cpx-carto-new from SMA1974-279 used for geothermobarometric calculations. The red dots on the profiles are the points used for the geothermobarometric calculations (see Table S-20).

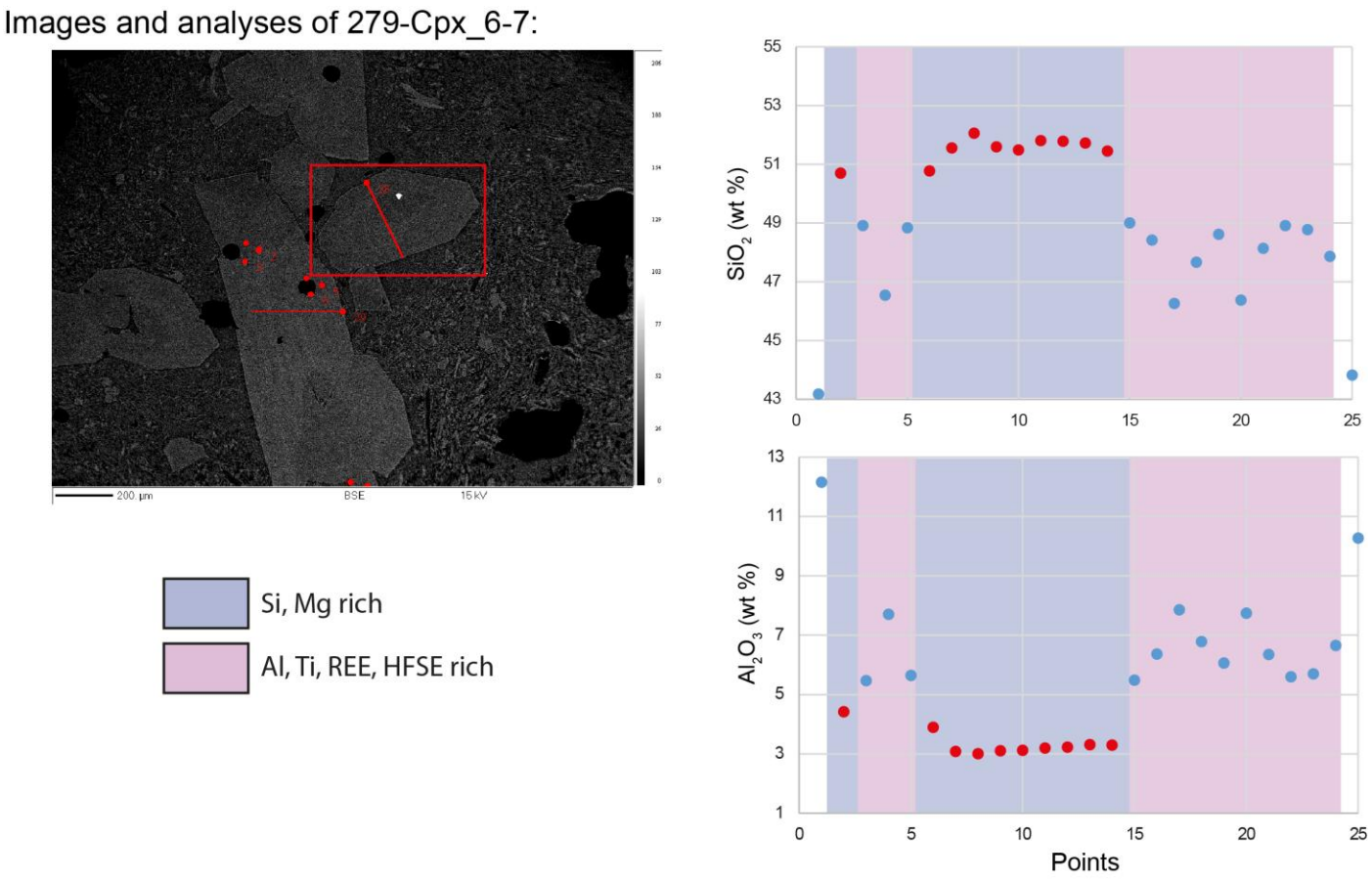

Figure S-18 BSE images and analysis profiles of Cpx6-7 from SMA1974-279 used for geothermobarometric calculations. The red dots on the profiles are the points used for the geothermobarometric calculations (see Table S-20).

Supplementary Information References

Barrat, J.A., Keller, F., Amossé, J., Taylor, R.N., Nesbitt, R.W., Hirata, T. (1996) DETERMINATION OF RARE EARTH ELEMENTS IN SIXTEEN SILICATE REFERENCE SAMPLES BY ICP-MS AFTER TM ADDITION AND ION EXCHANGE SEPARATION. *Geostandards Newsletter* 20, 133–139. https://doi.org/10.1111/j.1751-908X.1996.tb00177.x

Borghini, G., Fumagalli, P., Rampone, E. (2017) Partial melting of secondary pyroxenite at 1 and 1.5 GPa, and its role in upwelling heterogeneous mantle. *Contributions to Mineralogy and Petrology* 172, 70. https://doi.org/10.1007/s00410-017-1387-4

Brunelli, D., Verhoest, L., Ligi, M., Hemond, C., Maia, M., Soltanmohammadi, A., Lugli, F., Nonnotte, P., Cipriani, A. (2025) Large melt diversity at a mid-ocean ridge thermal low. *Science Advances* 11. https://doi.org/10.1126/sciadv.adv4654

Condamine, P., Couzinié, S., Fabbrizio, A., Devidal, J.-L., Médard, E. (2022) Trace element partitioning during incipient melting of phlogopite-peridotite in the spinel and garnet stability fields. *Geochimica et Cosmochimica Acta* 327, 53–78. https://doi.org/10.1016/j.gca.2022.04.011

Condamine, P., Médard, E. (2014) Experimental melting of phlogopite-bearing mantle at 1 GPa: Implications for potassic magmatism. *Earth and Planetary Science Letters* 397, 80–92. https://doi.org/10.1016/j.epsl.2014.04.027

Condamine, P., Médard, E., Devidal, J.-L. (2016) Experimental melting of phlogopite-peridotite in the garnet stability field. *Contributions to Mineralogy and Petrology* 171, 95. https://doi.org/10.1007/s00410-016-1306-0

Cotten, J., Le Dez, A., Bau, M., Caroff, M., Maury, R.C., Dulski, P., Fourcade, S., Bohn, M., Brousse, R. (1995) Origin of anomalous rare-earth element and yttrium enrichments in subaerially exposed basalts: Evidence from French Polynesia. *Chemical Geology* 119, 115–138. https://doi.org/10.1016/0009-2541(94)00102-E

Danyushevsky, L.V., Plechov, P. (2011) Petrolog3: Integrated software for modeling crystallization processes: PETROLOG3. *Geochemistry, Geophysics, Geosystems* 12, n/a–n/a. https://doi.org/10.1029/2011GC003516

Duvernay, T., Jiang, S., W. Ball, P., Davies, D.R. (2024) Coupled Geodynamical-Geochemical Perspectives on the Generation and Composition of Mid-Ocean Ridge Basalts. *Geochemistry, Geophysics, Geosystems*. https://doi.org/10.22541/essoar.169711689.99250544/v1

Grégoire, M., Bell, D., Le Roex, A. (2002) Trace element geochemistry of phlogopite-rich mafic mantle xenoliths: their classification and their relationship to phlogopite-bearing peridotites and kimberlites revisited. *Contributions to Mineralogy and Petrology* 142, 603–625. https://doi.org/10.1007/s00410-001-0315-8

Hellebrand, E. (2002) Garnet-field Melting and Late-stage Refertilization in "Residual" Abyssal Peridotites from the Central Indian Ridge. *Journal of Petrology* 43, 2305–2338. https://doi.org/10.1093/petrology/43.12.2305

Kendrick, M.A., Hemond, C., Kamenetsky, V.S., Danyushevsky, L., Devey, C., Rodemann, T., Perfit, M.R. (2017) Seawater cycled throughout Earth's mantle in partially serpentinised lithosphere. *Nature Geoscience* 10. https://doi.org/10.1038/ngeo2902

Kinzler, R.J. (1997) Melting of mantle peridotite at pressures approaching the spinel to garnet transition: Application to mid-ocean ridge basalt petrogenesis. *Journal of Geophysical Research: Solid Earth* 102, 853–874. https://doi.org/10.1029/96JB00988

Lambart, S. (2017) No direct contribution of recycled crust in Icelandic basalts. *Geochemical Perspectives Letters* 4, 7–12. https://doi.org/10.7185/geochemlet.1728

Marschall, H.R., Wanless, V.D., Shimizu, N., Pogge Von Strandmann, P.A.E., Elliott, T., Monteleone, B.D. (2017) The boron and lithium isotopic composition of mid-ocean ridge basalts and the mantle. *Geochimica et Cosmochimica Acta* 207, 102–138. https://doi.org/10.1016/j.gca.2017.03.028

Mollo, S., Putirka, K., Misiti, V., Soligo, M., Scarlato, P. (2013) A new test for equilibrium based on clinopyroxene–melt pairs: Clues on the solidification temperatures of Etnean alkaline melts at post-eruptive conditions. *Chemical Geology* 352, 92–100. https://doi.org/10.1016/j.chemgeo.2013.05.026

Neave, D.A., Putirka, K.D. (2017) A new clinopyroxene-liquid barometer, and implications for magma storage pressures under Icelandic rift zones. *American Mineralogist* 102, 777–794. https://doi.org/10.2138/am-2017-5968

Pertermann, M., Hirschmann, M.M., Hametner, K., Günther, D., Schmidt, M.W. (2004) Experimental determination of trace element partitioning between garnet and silica-rich liquid during anhydrous partial melting of MORB-like eclogite. *Geochemistry, Geophysics, Geosystems* 5, 2003GC000638. https://doi.org/10.1029/2003GC000638

Putirka, K. (1999) Clinopyroxene + liquid equilibria to 100 kbar and 2450 K. *Contributions to Mineralogy and Petrology* 135, 151–163. https://doi.org/10.1007/s004100050503

Putirka, K.D. (2008) Thermometers and Barometers for Volcanic Systems. *Reviews in Mineralogy and Geochemistry* 69, 61–120. https://doi.org/10.2138/rmg.2008.69.3

Sun, S. -s., McDonough, W.F. (1989) Chemical and isotopic systematics of oceanic basalts: implications for mantle composition and processes. *Geological Society, London, Special Publications* 42, 313–345. https://doi.org/10.1144/GSL.SP.1989.042.01.19

Van Der Zwan, F.M., Devey, C.W., Hansteen, T.H., Almeev, R.R., Augustin, N., Frische, M., Haase, K.M., Basaham, A., Snow, J.E. (2017) Lower crustal hydrothermal circulation at slow-spreading ridges: evidence from chlorine in Arctic and South Atlantic basalt glasses and melt inclusions. *Contributions to Mineralogy and Petrology* 172, 97. https://doi.org/10.1007/s00410-017-1418-1

Wang, W., Kelley, K.A., Li, Z., Chu, F., Dong, Y., Chen, L., Dong, Y., Li, J. (2021) Volatile Element Evidence of Local MORB Mantle Heterogeneity Beneath the Southwest Indian Ridge, 48°–51°E. *Geochemistry, Geophysics, Geosystems* 22, e2021GC009647. https://doi.org/10.1029/2021GC009647

Wieser, P.E., Kent, A.J.R., Till, C.B. (2023) Barometers Behaving Badly II: a Critical Evaluation of Cpx-Only and Cpx-Liq Thermobarometry in Variably-Hydrous Arc Magmas. *Journal of Petrology* 64, egad050. https://doi.org/10.1093/petrology/egad050

Workman, R.K., Hart, S.R. (2005) Major and trace element composition of the depleted MORB mantle (DMM). *Earth and Planetary Science Letters* 231, 53–72. https://doi.org/10.1016/j.epsl.2004.12.005

Yu, Z., Singh, S.C., Hamelin, C., Grenet, L., Maia, M., Briais, A., Petracchini, L., Brunelli, D. (2025) Deep mantle earthquakes linked to CO2 degassing at the mid-Atlantic ridge. *Nature Communications* 16, 563. https://doi.org/10.1038/s41467-024-55792-9

Zhou, J.-S., Wang, Q., Xing, C.-M., Ma, L., Hao, L.-L., Li, Q.-W., Wang, Z.-L., Huang, T.-Y. (2021) Crystal growth of clinopyroxene in mafic alkaline magmas. *Earth and Planetary Science Letters* 568, 117005. https://doi.org/10.1016/j.epsl.2021.117005